2012

Electron contamination modeling and skin dose in 6 MV longitudinal field MRIgRT: Impact of the MRI and MRI fringe field

Bradley Oborn
University of Wollongong, boborn@uow.edu.au

Peter E. Metcalfe
University of Wollongong, metcalfe@uow.edu.au

Martin Butson
University of Wollongong, butson@uow.edu.au

Anatoly B. Rosenfeld
University of Wollongong, anatoly@uow.edu.au

P J. Keall
University Of Sydney

Electron contamination modeling and skin dose in 6MV longitudinal field MRIgRT: impact of the MRI and MRI fringe field

B. M. Oborn[1,2], P. E. Metcalfe[2], M. J. Butson[1,2], A. B. Rosenfeld[2], P. J. Keall[3].
[1]Illawarra Cancer Care Centre (ICCC), Wollongong, NSW 2500, Australia.
[2]Centre for Medical Radiation Physics (CMRP), University of Wollongong, Wollongong, NSW 2500, Australia.
[3]Sydney Medical School, University of Sydney, NSW 2006, Australia.

Abstract

Purpose: In recent times, longitudinal field MRI-linac systems have been proposed for 6 MV MRI-guided radiotherapy (MRIgRT). The magnetic field is parallel with the beam axis and so will alter the transport properties of any electron contamination particles. The purpose of this work is to provide a first investigation into the potential effects of the MR and fringe magnetic fields on the electron contamination as it is transported towards a phantom, in turn, providing an estimate of the expected patient skin dose changes in such a modality.

Methods: Geant4 Monte Carlo simulations of a water phantom exposed to a 6 MV X-ray beam were performed. Longitudinal magnetic fields of strengths between 0 and 3 T were applied to a 30x30x20 cm^3 phantom. Surrounding the phantom there is a region where the magnetic field is at full MRI strength, consistent with clinical MRI systems. Beyond this the fringe magnetic field entering the collimation system is also modeled. The MRI-coil thickness, fringe field properties, and isocentric distance are varied and investigated. Beam field sizes of 5x5, 10x10, 15x15 and 20x20 cm^2 were simulated. Central axis dose, 2D virtual entry skin dose films, and 70 μm skin depth doses were calculated using high resolution scoring voxels.

Results: In the presence of a longitudinal magnetic field, electron contamination from the linear accelerator is encouraged to travel almost directly towards the patient surface with minimal lateral spread. This results in a concentration of electron contamination within the x-ray beam outline. This concentration is particularly encouraged if the fringe field encompasses the collimation system. Skin dose increases of up to 1000% were observed for certain configurations and increases above D_{max} were common. In non-magnetically shielded cases, electron contamination generated from the jaw faces and air column is trapped and propagated almost directly to the phantom entry region, giving rise to intense dose hot spots inside the x-ray treatment field. These range up to 1000% or more of D_{max} at the CAX, depending on field size, isocentre and coil thickness. In the case of a fully magnetically shielded collimation system and the lowest MRI field of 0.25 T, the entry skin dose is expected to increase to at least 40%, 50%, 65%, and 80% of D_{max} for 5x5, 10x10, 15x15, and 20x20 cm^2 respectively.

Conclusions: Electron contamination from the linac head and air column may cause considerable skin dose increases or hot spots at the beam central axis on the entry side of a phantom or patient in longitudinal field 6 MV MRIgRT. This depends heavily on the properties of the magnetic fringe field entering the linac beam collimation system. The skin dose increase is also related to the MRI-coil thickness, the fringe field, and the isocentre distance of the linac. The results of this work indicate that the properties of the MRI fringe field, electron contamination production and transport must be considered carefully during the design stage of a longitudinal MRI-linac system.

I. INTRODUCTION

Currently there are 2 working MRI-linac prototypes: a modified 6 MV Elekta accelerator merged with a modified 1.5 T Philips Achieva MRI system[1] and a 6 MV accelerator merged with a biplanar, low field (0.2 T) MRI[2]. A commercial Cobalt-60 device merged with a MRI is also under development[3]. These systems have the magnetic field of the MRI unit lying perpendicular or transverse to the linac x-ray beam direction. This results in numerous dose perturbation effects including the electron return effect, lateral dose shifting, cavity under and overdosing[4],[5],[6],[7],[8],[9] and potentially large entry and exit skin dose increases[10],[11]. These negative effects are usually reduced significantly

however in lower magnetic field systems, as the Lorentz-force perturbation is minor[9],[10]. In terms of engineering, the transverse MRI-linac system faces some issues with changes to the gun, waveguide and multileaf collimator operation[12],[13],[14],[15]. Magnetic shielding is required to reduce the effect of the MRI fields down to low enough levels for proper operation of the linac[14].

There have been some recent studies on the improved dosimetry that a parallel or longitudinal MRI-linac system would offer over the current transverse field systems[16]. In this case, the Lorentz-force perturbation acts in-line with the x-ray beam direction, resulting in no lateral dose shifting. As a result, there is no electron return effect (ERE) or over/underdosing at lung/tissue interfaces. Other positive dosimetry changes which occur in the presence of longitudinal magnetic fields were first reported by Bielajew in 1993[17]. These mainly include the narrowing of penumbral widths, which allows for a more conformal dose profile. When combined, these effects could further improve the already obvious benefits of this advanced form of image guided radiotherapy (IGRT).

However, one aspect of dosimetry changes in longitudinal MRIgRT has not been studied in any great depth: the effect of non-purged electron contamination. This is unlike a transverse field MRI-linac system where all electrons are swept from the x-ray beam by the transverse field. In a sufficiently strong longitudinal magnetic field, electron contamination will not scatter laterally away from its site of production. This has the effect of concentrating the electron contamination within the x-ray beam area and as a result skin dose increases. From the many studies on electron contamination, we know that the origin of the majority of electron contamination is spread between the flattening filter, secondary collimation devices and the air column which is irradiated by the x-ray beam between the patient surface and linac head[18],[19],[20],[21],[22],[23],[24],[25],[26],[27],[28],[29]. These locations project to inside the x-ray beam outline when transported (parallel to the CAX) down to the patient skin level. Two articles do briefly show a similar effect for a 10 MV photon beam of 10x10 cm^2[30],[31].

In the recent study by Kirkby *et al.*[16], the electron contamination component was considered to some degree in a Monte Carlo simulation. The dose scoring simulation considered a phase space input file which was generated without the presence of any magnetic field. The phase space file was located at 70 cm from the linac target and 30 cm from isocentre. This allowed true tracking of electrons over about 10 cm before arriving at the patient skin surface. The focus of this work was not related to skin dose and electron contamination. Hence no estimates of the skin dose were presented. The authors did however comment that this approach may have some effect on the accuracy of simulating electron contamination.

In this work, we present a first approach to estimating the skin dose increases expected in 6 MV longitudinal field MRIgRT by careful consideration of the electron contamination transport. Two different arrangements are considered for the MRI-linac design, which reflect the potential real prototype longitudinal field MRI-linac system; the first is an 'integrated' system where the linac side MRI coil is located immediately next to the linac collimation components while the second is a 'separated' system where there is a distinct air gap between the MRI coil and the linac collimation components.

II. MATERIALS AND METHODS

Longitudinal MRI-linac designs

At present, there are plans to construct a Longitudinal MRI-linac system by the Fallone group[32]. There is also a funded project developing a split bore MRI linac system for inline and perpendicular orientation experiments at Liverpool Hospital in Sydney, Australia. In both these designs, there is a split bore MRI system with the linac located along the magnetic field or coil axis and lying outside of the coil. A schematic diagram is shown in figure 1 for two variations of this model. In order to treat a patient, the x-ray beam must travel through a region of fringe field

outside the coil area (B_{FF}) and then through the coil central hole where it will be exposed to the full MRI strength magnetic field (B_{MRI}). There is the strong possibility that the longitudinal MRI-linac system will require an isocentre of greater than 100 cm for several reasons. The main reason is that the beam collimation system, e.g. jaws and mulitleaf collimators (MLCs) will most likely not be contained inside the MRI-coil, as the bore size will be too small. An increase in the distance to the linac will have the positive effect of lowering the magnetic field effects induced on the linac. However this will lead to dose reductions due to the inverse square radiation fluence drop-off at the greater isocentre distances. Also, if any collimation components are further away from the patient, their position errors at isocentre and geometric penumbra will be magnified.

For the purposes of this first study on the electron contamination, two different MRI-linac systems were modeled: an 'integrated' system and a 'separated' system (see figures 1 (a) and 1 (b)). In the integrated designs, the linac-side MRI coil (or potential coil outer boundaries) always extended to just 60 cm from the linac target, i.e. almost immediately below the level of the MLC's of a conventional Varian 2100C linac. This arrangement was designed to reflect a MRI-linac design where the two devices were as close as possible together, mainly to produce a minimum isocenter distance machine. In the separated system, there was some degree of an air gap between the linac and MRI coil boundary. This design was aimed at allowing some form of magnetic decoupling or separation of the linac from the MRI without perturbing the MRI field quality near the patient. Note that the actual superconducting coils can be located anywhere inside the shown MRI coil boundary. The MRI coil regions shown in figure 1 represent the boundaries of where the actual coils could be. The linac-side outer coil boundary was designed to represent approximately the location where the MRI magnetic field starts to drop off. The term MRI coil is now henceforth used to represent the region of where the actual coils may be placed.

In both systems the MRI coil separation was fixed at 40 cm. This would ultimately allow for a maximum patient diameter and imaging field of view of something comparable to 40x40 cm^2, provided the MRI design has a good uniformity between the coils. This value was fixed for all simulations and was simply a first guess at what the coil separation might be. The next two sections describe the simulations performed for each of the two designs.

Integrated design simulations

In the integrated design simulations four different isocentre distances were simulated which correspond to four different MRI coil thicknesses (or coil regions). In each case, however, the outer edge of the linac side MRI coil boundary was located at 60 cm from the linac target (see figure 2)). In this set of simulations, the isocentre distances were set at 100, 120, 150, and 180 cm. These correspond to MRI coil thicknesses of 20, 40, 70 and 100 cm. For each of these arrangements, the magnetic fields applied consisted of a uniform region between the outer edges of the MRI coils (B_{MRI}) and some sort of fringe field extending beyond this (B_{FF}). The values of B_{MRI} are 0, 0.25, 0.5, 0.75, 1, 1.5, and 3 T. In figure 2 B_{MRI} was nominally chosen as being 1 T. Various fringe fields were then adjoined to each of these B_{MRI} values. The details of the fringe fields are described in a separate section below.

Separated design simulations

In the separated design simulations, only an isocentre distance of 180 cm was simulated. However four different MRI coil thicknesses were applied of 20, 40, 60 and 80 cm. In each case, the outer edge of the linac side MRI coil moved closer to the linac target (see figure 3). Physically, this reflected a MRI-linac system with a varied air gap between the two components. The increased isocenter distance was desirable to help lower the magnetic field effects on the linac operation. Changing the thickness of the MRI coils was designed to allow potentially stronger MRI fields. In terms of

electron contamination, it exposes any effects related to accumulation of air generated electron contamination trapped inside the MRI coil bore and propagating to the patient level. For each of these arrangements, the magnetic fields applied consisted of a uniform region between the outer edges of the MRI coils (B_{MRI}) and the fringe field extending beyond this (B_{FF}). The values of B_{MRI} and B_{FF} were the same as the integrated design simulations and in figure 3 B_{MRI} was nominally chosen as being 1 T.

MRI fringe field properties: B_{FF}

The fringe field of a commercial MRI unit depends on whether it has active shielding or not and on the bore size. For actively shielded systems a wide range of fringe fields are possible. In this work we modeled 5 different potential fringe fields with a broad range of properties to cover a wide range of potential designs, including the limits of B_{MRI} and 0 T. Each of these fringe fields were applied to both the integrated and separated system simulations. These included:

1. $B_{FF} = 0$ T: i.e., zero fringe field. This field was designed to replicate the effect of a fully shielded linac collimation system.
2. $B_{FF} = 0.06$ T: i.e. a constant $B_z = 0.06$ T field above MRI-coils. This was designed to match the limit of operation of MLC motors[15])
3. $B_{FF} = 1/r^5$ drop off from coil edge: This consisted of only a B_z component which dropped off as $1/r^5$ from B_{MRI} at the coil edge. There is mention in the recent work by St Aubin *et al.*[14], that without magnetic shielding the uniformity of B_{MRI} in the imaging field of view is much higher. This type of fringe field would exist in a non-shielded case where the MRI unit also has active magnetic field shielding in the form of reverse coils outside the main coils.
4. $B_{FF} = 1/r^2$ drop off from the edge of the coil: The same as (3) however this reflected a non-shielded MRI system and non-shielded linac collimation system.
5. $B_{FF} = B_{MRI}$: i.e. full MRI strength magnetic field extending up to the phase space file level. This fringe field was designed to quantify the skin dose changes in a system where the collimation system may be fully encompassed by the MRI field. Physically, this would occur if the collimation system is enclosed by the coil.

For this first study, we deliberately only assigned a B_z component in the fringe fields. In otherwords for each fringe field the components B_x and B_y are set to 0 T. Future studies would include the B_x and B_y components once designs are drawn and modeled. We note here that in a real MRI system, the B_x and B_y components are approximately zero near the bore central axis of the fringe field. Off axis values of B_x and B_y will have some magnitude. Their directions due to the symmetrical nature of the coil will point towards the central axis. It is expected that this would in fact encourage electrons to focus towards the central axis if B_x and B_y are strong enough, much like how the earth's magnetic field encourages charged particles to focus near the poles. At the same time however, we note that if the change in B_z is strong enough when combined with some small B_x or B_y then some electrons may be reflected by the "magnetic mirror" effect[33]. This phenomenon was observed in the work by Chen *et al.* in 2005[31].

Monte Carlo simulations

The Monte Carlo simulations were performed using Geant4.9.4[34]. The beam modeled was a 6 MV (Varian 2100C) photon beam[35]. The accuracy of this linac head model has been confirmed in previous work[11] for the Geant version 4.9.1. The same benchmarking measurements were repeated with the lastest version and results were essentially identical. For all simulations, a phase space file was used as the input particles. This was located at a plane 25 cm away from the linac target. In the simulation which produced the phase space file, there was no magnetic field

present. This was deliberate and was intended to reflect a shielded portion of the linear accelerator head. This phase space file consisted of 2x10^8 particles with no bremsstrahlung splitting. In generating this phase space file the Monte Carlo particle step and cutoff parameters were set at 0.2 mm throughout the entire linac head geometry.

Simulation phantom

The simulation phantom consisted of a 30x30x20 cm^3 water block. This has a SSD of 10 cm less than the isocentre distance, which depended on the particular simulations performed. Scoring voxels included two types. Firstly there were central axis square cross-sectioned voxels of 0.5 mm z-thickness. The cross-sectional area was 4% of the x-ray beam field size at the system isocentre, and they were used to extract CAX percentage depth-dose profiles. Secondly, high resolution virtual skin dose films were present across the entire entry surface. These were 10 μm thick layers from 0 to 0.5 mm depth (i.e. 50 layers total). In each of these layers the x-y pixel resolution was 1x1 mm^2. The two films between 60-70 μm and 70-80 μm were simply averaged to provide a full 2D virtual skin dose film of the beam entry region. This was done to obtain an effective skin dose at depth of 70 μm, as described in the ICRP Report 59[36]. The Monte Carlo particle step and cutoff parameters were set to 5 μm in the scoring voxels while 0.2 mm was used everywhere else (phantom body, surrounding air). This approach of using high resolution voxels and 5 μm step and cut values has been shown to be accurate in predicting entry and skin dose values as compared to Attix chamber measurements from some of our own previous work[11], and that of Devic et al[37]

For each simulation the dose per primary particle fired from the phase space file (above the jaws) was recorded. For each dose value however the values where scaled or normalized to set the dose at 30 mm depth to be "95%" in the CAX voxel simulations (this projects to 100% at 15 mm depth). This allows for a direct comparison across the different magnetic fields, field sizes, and isocentre distances. The virtual film voxels then simply had the same factors applied to them in order to extract meaningful dose values.

Typically enough particle histories were simulated to achieve less than 5% statistical error in the CAX voxels located near D_{max}. This was around 0.5, 0.7, 1.2, and 1.7 billion histories for the 100, 120, 150, and 180 cm isocentre simulations respectively.

III. RESULTS

A. Visualization of non-purged electron contamination

The gross effect of the longitudinal magnetic field on the electron contamination properties can be explained by a simple visual study in the Monte Carlo environment. Figures 4 and 5 show the paths of the electron contamination from a 10x10 cm^2 6 MV photon beam as it travels towards a phantom surface in the integrated and separated system respectively. In each figure, a total of 100000 particles have been fired from a phase space located at z=25 cm from the x-ray target, i.e. above the secondary collimator jaws and the value of B_{MRI} when applied is 1 T. In part (a) of each figure, no magnetic field is present and the resultant electron paths are mostly forward directed. However they can undergo large lateral deflections when interacting with air molecules. For the integrated system shown (fig 4), parts b, c and d show how the electron contamination is radically altered by the presence of B_{MRI} and B_{FF}. In (b) there is no fringe field (B_{FF} = 0 T). However once electrons enter the MRI coil region, i.e. into a magnetic field of B_{MRI}, we see a dramatic path change and a distinct lack of lateral spread of the contamination. In (c) and (d) we see the inclusion of $B_{FF} = 1/r^5$ and $B_{FF} = 1/r^2$. These fringe fields penetrate strongly into the collimation system and so essentially alter the electron paths as soon as they are created. This leads to a distinct lack of lateral spread of the electron contamination. It should be noted that figure 4 is of the 100 cm isocentre distance. For the other simulated

integrated systems of 120, 150, 180 cm, the fringe fields start at the z = 60 cm plane. The main difference is that any further air-generated contamination produced inside the B_{MRI} region will also be encouraged to travel towards the phantom surface. This would result in even greater numbers of electrons arriving at the phantom surface with minimal lateral spreading.

Figure 5 parts (a) to (e) show how the electron contamination is altered by a changing coil thickness in the separated system. The fringe field is B_{FF} = 0 T in each of these parts. It is clear that the deeper the MRI coils, the greater the amount of electron contamination which will arrive inside the x-ray beam area. Hence the greater the skin dose increase. In part (f) we see the effect of including a fringe field of $1/r^5$ to the 80 cm coil thickness system, i.e. very strong encouragement of electrons to travel towards the phantom surface. Section B provides quantitative insight into the skin dose changes at the beam CAX, while section C will quantitatively analyse how the contamination was spread across the entry surface.

B. Central Axis Skin Dose in the Entry Region

Integrated systems

Figure 6 displays the central axis depth dose profiles for the integrated system simulations. Note that the dose points are absent in the first 1 mm depth. This is where the scoring films are located, which in turn is used to extract the 70 μm skin doses and films (part C). Figure 8 summarises the 70 μm skin dose at the beam central axis for each of the integrated system simulations. Figure 10(a) also shows the skin doses for the fully magnetically shielded case. The first and most striking feature of figures 6 and 8 are the massive increases predicted for the non-shielded fringe fields, $B_{FF} = 1/r^5$, $1/r^2$, and B_{MRI}. The CAX skin dose quickly becomes greater than the value of D_{max} as B_{MRI} increases above 0.25 T. This is because of the significant longitudinal magnetic field entering the beam collimation system. The magnetic field traps almost all of the electron contamination and forces it to travel directly to the phantom surface (as seen in the previous figures). Next, we note that even the shielded fringe fields B_{FF} = 0 and 0.06 T give rise to clinically significant skin dose changes at the CAX. There is a quick increase in skin dose up to about 0.5 T where it levels off. This is related to all the electron contamination being trapped and not allowed to laterally diverge above approximately 0.5 T. There is also a clear separation between the shielded and non-shielded fringe field results. This is a result of the differences in magnitude of the fringe field near the linac collimation system between the two groups. In the unshielded fringe fields, the entire collimation system is exposed to far greater B_z values (as can be seen in figure 2). As the isocenter distance increases, this fringe field magnitude remains constant, hence the consistant separation at all isocentre distances.

There are also some trends present in figure 8 that are not so obvious:

1. a reduction in the maximum skin dose versus beam field size for the most penetrating fringe fields (for 10x10, 15x15, and 20x20 cm^2: this is opposite to the conventional phenomenon where skin dose increases with beam field size (at zero magnetic field). For the lower penetrating magnetic fields this does hold however.
2. a subtle change in the behavior at 5x5 cm^2 as compared the larger field sizes (for the penetrating fringe fields B_{FF} = 1/r2, 1/r5, and B_{MRI}): there is a reduction in maximum skin dose as compared to the trend just mentioned.

The reason for these two features is related to the make up of the electron contamination which falls on the CAX scoring voxel cross section (4% of the field size). At low magnetic fields (which penetrate the collimation system) contamination will still laterally diverge to some extent and so the dose at CAX comes from electrons scattered from the jaw faces and from the air-column, mostly above the CAX voxel area. At the higher fringe fields the contamination begins to track down much more parallel to the CAX. As a result, more jaw-face contamination starts to fall outside

the CAX voxel cross section (when traced parallel down to the phantom surface, the exposed jaw area falls outside the CAX voxel cross-section) and so the ratio of what gives rise to the CAX dose becomes more dependent on the air-column contamination. Hence we see the small reduction in maximum skin doses with increasing field size. However, an exception is the 5x5 cm^2 case as mentioned above. In this case the jaws faces are very close to the projected irradiated air-column above the CAX voxel (the volume which gives rise to this dose component at CAX). Visualization studies showed us that in fact some upstream (above jaws) air-column contamination is absorbed by the jaws and so lowers this component as compared the the larger beam field sizes where the above jaw air-column contamination is free to pass through the jaws with minimal absorption. These small but readily understandable effects are really as a result of having the fringe field consisting of only a B_z component. We expect that in the case of a more realistic fringe field that there would be much more complex changes occurring as lateral (B_x and B_y) components may give rise to the magnetic mirror effect that would potentially absorb more air generated contamination into the jaw faces, however also focus contamination back into the beam cross section due to the shape of the fringe field. It should be noted here that these results are of the skin dose at the beam CAX. The previous visualization study gives us reason to expect dose hot spots near the CAX and so these values may be greater than those off-axis. Section C describes full virtual surface films which describes the doses away from CAX

Separated systems

Figure 7 and figure 9 show the central axis depth dose profiles and a summary of the 70μm skin dose at the beam central axis for the separated systems. Figure 10(b) displays the skin doses for the fully magnetically shielded case. Similar to the integrated systems, considerable CAX skin dose are observed for the non-shielded fringe fields, and still clinically significant changes are reported for the shielded cases. In the case of $B_{FF} = B_{MRI}$, the skin doses should all be the same for each respective coil thickness as the magnetic field is the same in each case. This is shown by the close alignment of the $B_{FF} = B_{MRI}$ curves. These represent an absolute worst-case senario if the fringe field is equal to B_{MRI} and extends all the way up to the phase space file level.

Also similar to the integrated system, there are some subtle changes in the trends of the maximum skin doses between the highly penetrating and weakly penetrating fringe fields. This time however, the extended isocentre distance means that the projected jaw faces are closer to the CAX voxel area and so there is more dependence on the field size. Now we generally see that increasing the field size increases the maximum skin doses. Again however the further exception holds at 5x5 cm^2 where at $B_{FF} = B_{MRI} = 3$ T the skin dose does not follow the trend of 10x10, 15x15, 20x20 cm^2.

C. Virtual Skin Dose Films in the Entry Region

The results of this section provide full 2D virtual films of the 70 μm skin dose. These are designed to verify the predictions of the visualization study into how the concentration of electron contamination changes across the phantom surface and of the extent of the expected CAX dose hot spots. Figures 11 and 12 display the virtual films for the integrated and separated systems, respectively. As predicted, the films show strong CAX dose hot spots in both systems, particularly for the non-shielded fringe fields. A clear rectangular hot spot is seen. Essentially this is a projection of the beam field size as it was at the jaw level. Physically it represents contamination from inside the collimation area at the jaw level being propagated almost directly towards the phantom surface as soon as it is created. We therefore see a rectangular hot spot as the x and y-jaws are at different z-planes. Correspondingly we also see that the size of the hot spot is larger for the shorter isocentre systems. For the shielded fringe fields we see

the expected clinically significant hot spots around CAX. For the $B_{FF} = 0$ T, the electron contamination undergoes its natural divergent path until the z-level of the MRI coil edge where it then enters full B_{MRI} magnetic field. From this point on the contamination travels almost straight towards the phantom surface. Hence we see a square hot spot rather than a rectangular one. For the $B_{FF} = 0.06$ T, the contamination is slightly affected as soon as it is created. The helical radius of gyration of the electrons is (13.6 cm for 2 MeV electron in 0.06 T) large enough that the beam cross-section at the jaw level is not fully preserved. Hence we see a different, somewhat oval shaped hot spot around CAX. The oval shape most likely corresponds to some electrons from the upper y-jaws being slightly laterally shifted by the larger radius of gyration and then blocked by the lower x-jaws. They are then removed from the projected hot spots.

IV. DISCUSSION

The skin dose values reported in this work were predicted via Monte Carlo simulation. As there was no operational longitudinal MRI-linac system accessible we were unable to experimentally verify these predictions. Therefore we need to justify the Monte Carlo results. There are several pieces of evidence that directly support the accuracy of the simulations in predicting skin doses. The first is of the 70μm skin doses without a magnetic field. Our values are consisent with those derived by accurate experiental (Attix chamber and extrapolated film) methods by Devic et al[37] for all the field sizes simulated. Secondly, there is the validity in the presence of magnetic fields: we have performed Monte Carlo skin dose calculations at various surface angles, field sizes and transverse magnetic fields[11],[10]. When relaxed to lower resolution, these results matched well to experimental data from the UMC (Utrecht) MRI-linac system[6]. Thirdly, we note the experimental results of Litzenberg et al[30] which clearly shows the surface dose is much higher than the photon dose when exposed to a 0.5 - 3 T longitudinal magnetic field. This has also been verified with Monte Carlo simulations[31]. This experimental system has a longitudinal fringe field and could be considered as being similar to a scaled down longitudinal MRI-linac system. These authors explain this effect seen directly as being air-generated electrons trapped by the nearby fringe field region. In our work we had an additionally larger air volume, and further, the jaw-generated contamination is present. In summary we expect to see skin doses far greater than D_{max} doses.

Perhaps the most significant or consequencial part of this study is the representation of the fringe field. Electron contamination is easily pertubed by a magnetic field of around 0.1 T, such as the values near where the linac may be placed outside the MRI system. In this work the direction is fixed with a B_z component only. Hence there will be no modelling of the magnetic mirror effect or of magnetic focusing (like the earth's field collecting charged particles at the poles). These two effects would counter act each other. The resultant amount of contamination travelling towards a patient would be dependent on which effect is stronger, and then also on the size of the air column above the patient. The latter region is somewhat exempt from these two processes as the magnetic field will consist almost entirely of a B_z component as it is the requirement of the MRI scanner - to be highly uniform in the B_z component surrounding the patient. In future work we aim to investigate these more realistic fringe fields by using magnetic field data exported from magnetic field studies of realistic MRI-linac designs. We expect the results to be similar for the low penetrating fringe fields investigated as the contamination arises primary from the immediate air-column above the patient, however may be significantly different for the highly penentrating fringe field designs if the magnetic mirror effect is strong. We also note two things regarding translating this work to a real MRI-linac system. Firstly, that it is expected that multi-leaf collimators (MLC's) would be most likley used to collimate the x-ray beam. These would act to collect a lot of the jaw generated contamination, however also introduce some as well. And secondly, that the most important underlying skin dose increases that would be expected is that of around D_{max}. That is, in the case

where any contamination causes skin dose to be greater than D_{max}, then sufficent entry side bolus would be applied to collect the contamination, bringing the patient skin dose to something in the order of D_{max}. This may seem clinically too high, however is strongly distributed or reduced once multiple field treamtments such as IMRT or arc therapy are used. Such treatment modalities are the aim for MRI-linac radiotherapy as it compliments the image guidance offered by the MRI-linac.

IV. CONCLUSION

This work presents a first study on the impact of accurately modeling electron contamination in various prototype longitudinal field MRI-linac systems using Monte Carlo simulations. Entry skin doses were calculated for integrated and separated MRI-linac designs modeled with changing MRI field strength, MRI-coil thickness, isocentre distance and the type of MRI fringe field. For beam field sizes of 5x5, 10x10, 15x15 and 20x20 cm^2 CAX skin doses and full 2D virtual entry skin dose films were produced. Undesirably high entry skin doses were reported, as the longitudinal magnetic field traps electron contamination and forces it to travel directly towards the patient surface without undergoing its natural lateral divergence or spread. The final skin dose estimates were heavily dependent on the properties of the MRI fringe field entering the linac collimation system. However even in a fully magnetically shielded collimation system, clinically significant skin doses were still reported. We expect that more realistic fringe fields (i.e. containing B_x and B_y components) would give rise to more complex changes to the skin dose as the magnetic mirror effect can act to both purge and focus contamination. It is expected that future Monte Carlo simulations of the type presented in this work could play an invaluable role in advancing longitudinal field MRI-linac designs. These include modelling more realistic fringe fields and investigating strategies to reduce the undesirable increased skin dose.

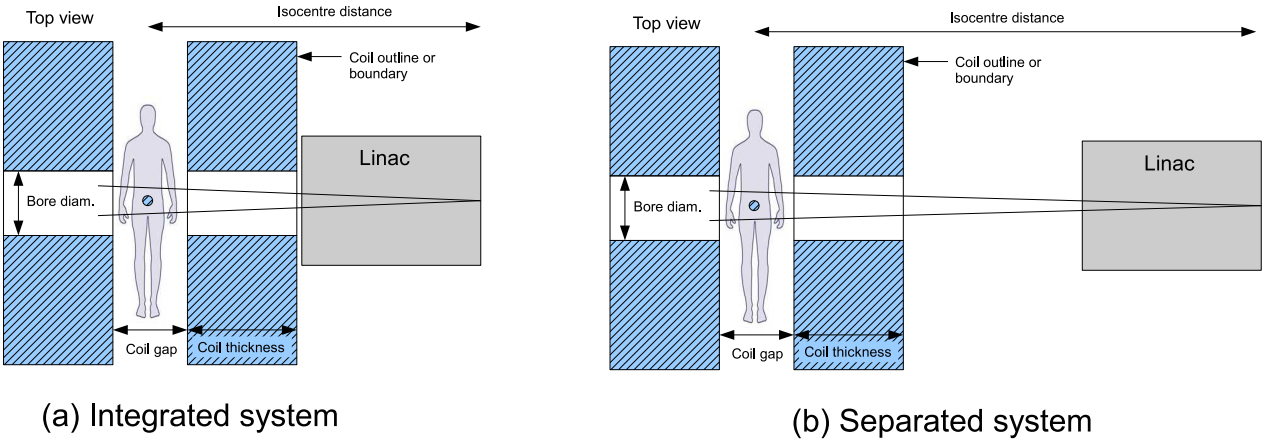

Figure 1: Schematic diagram of the basic longitudinal MRI-linac system. A split-bore MRI is coupled with a nearby linac which produces its x-ray beam through the open coil bore and parallel with the magnetic field direction. The patient will lie between the MRI coils. Two different models were simulated in this work: an 'integrated' and a 'separated' system. In the integrated system shown in part (a), the linac is mounted immediately adjacent to the outer edge of the MRI coil such that the full MRI strength magnetic field (B_{MRI}) is present near the linac collimation system. In part (b) the separated system is shown. This system allows for a distinct air-gap or physical distance between the two components. This system is aimed at lowering the magnetic fringe field (B_{FF}) which penetrates the linac collimation system by shear physical distance.

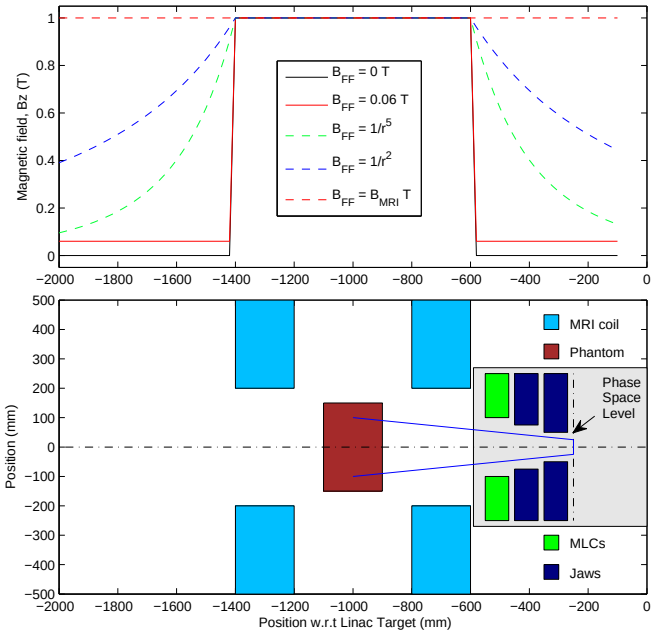

(a) ISO = 100 cm

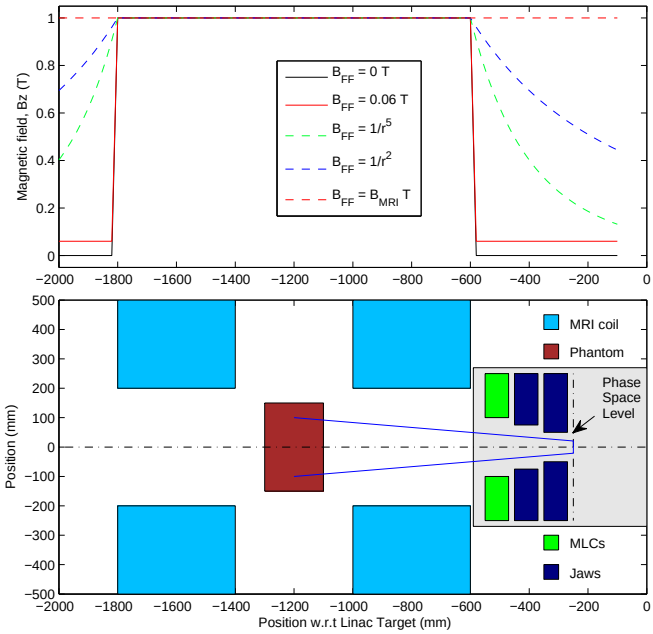

(b) ISO = 120 cm

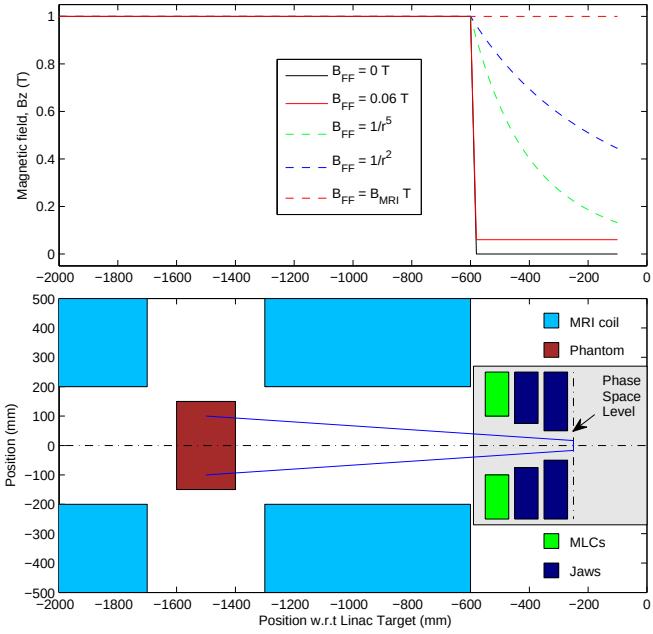

(c) ISO = 150 cm

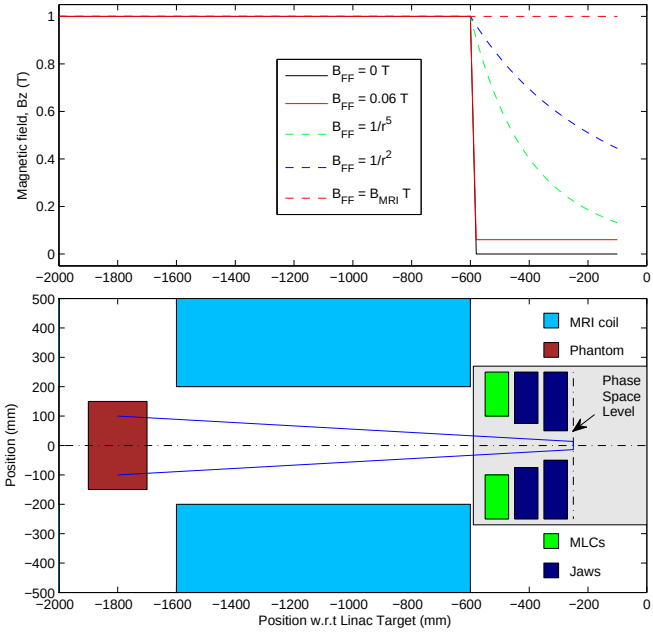

(d) ISO = 180 cm

Figure 2: Schematic diagram of the different simulated 'integrated' longitudinal MRI-linac systems, where the beam collimation system is always adjacent to the MRI coils. In parts (a), (b), (c) and (d) we see the 100, 120, 150 and 180 cm isocentre systems, respectively. These, in turn, have MRI-coil thicknesses of 20, 40, 70 and 100 cm. In each part the top figure indicates the magnetic field in the z-direction. Inside the outer MRI coil edges, the magnetic field shown is equal to B_{MRI}, in this case 1 T is chosen. In the regions outside the MRI-coils, the various fringe fields, B_{FF} are shown.

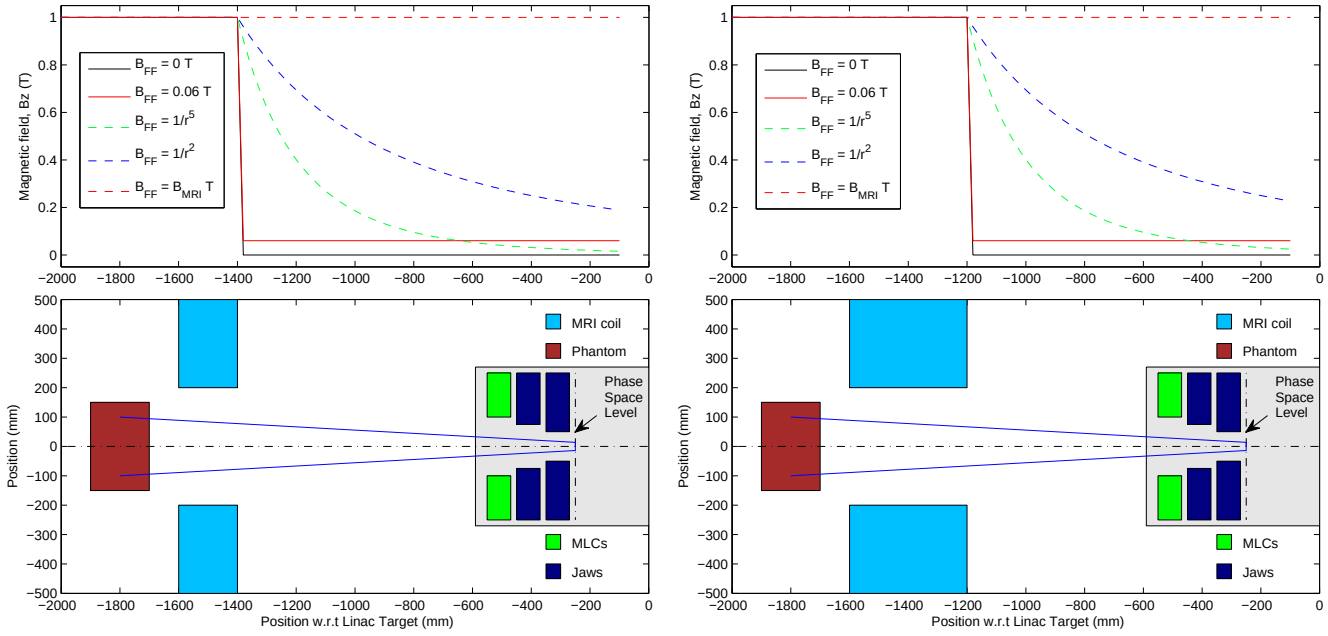

(a) 20 cm Coil

(b) 40 cm Coil

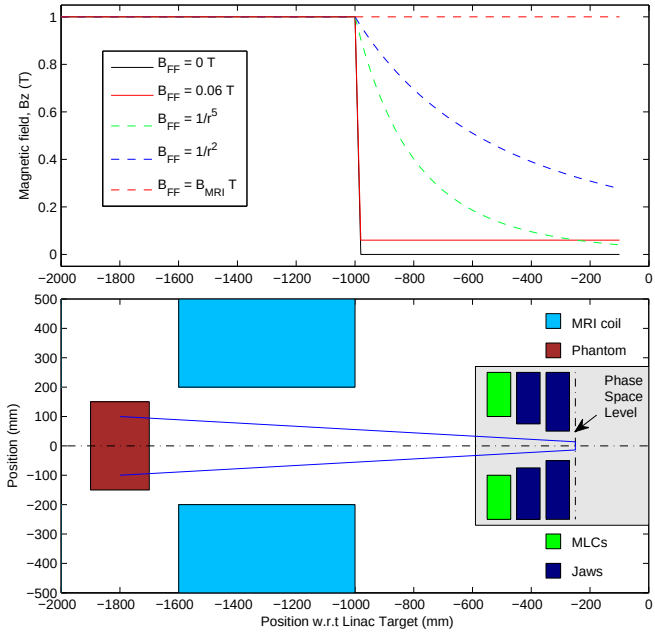

(c) 60 cm Coil

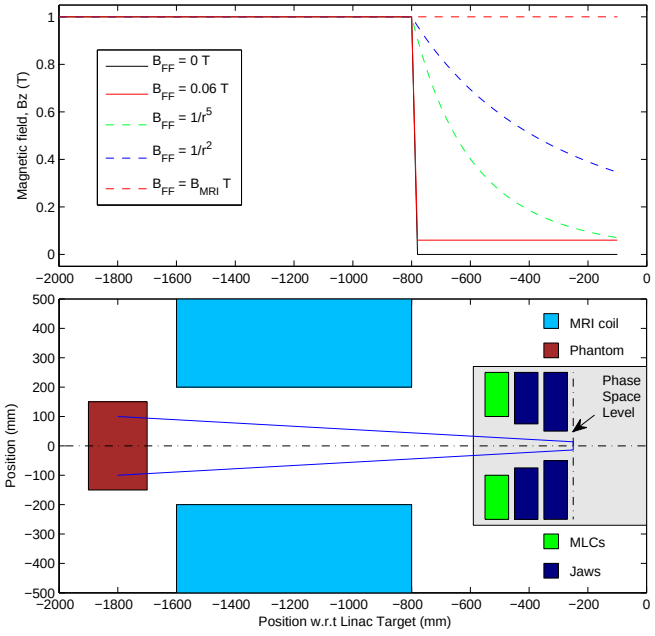

(d) 80 cm Coil

Figure 3: Schematic diagram of the different simulated 'separated' longitudinal MRI-linac system where the beam collimation system is separated from the MRI coil by an air gap. The isocentre distance is fixed at 180 cm. Shown are the 20, 40, 60 and 80 cm MRI coil thicknesses in parts (a), (b), (c) and (d), respectively. In each part, the top figure indicates the magnetic field in the z-direction. Inside the outer MRI coil edges the magnetic field shown is equal to B_{MRI} in this case 1 T is chosen. In the regions outside the MRI-coils the various fringe fields, B_{FF} are shown.

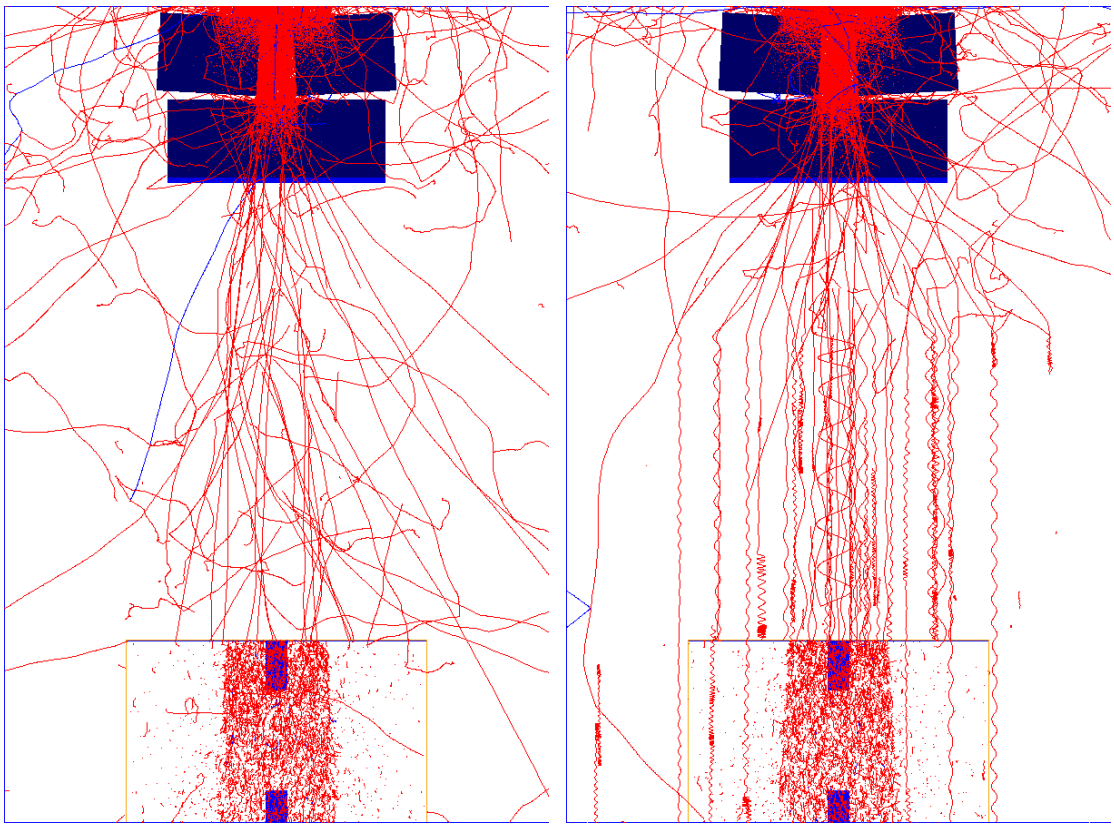

(a) $B_{MRI} = 0$ T

(b) $B_{MRI} = 1$ T, $B_{FF} = 0$ T

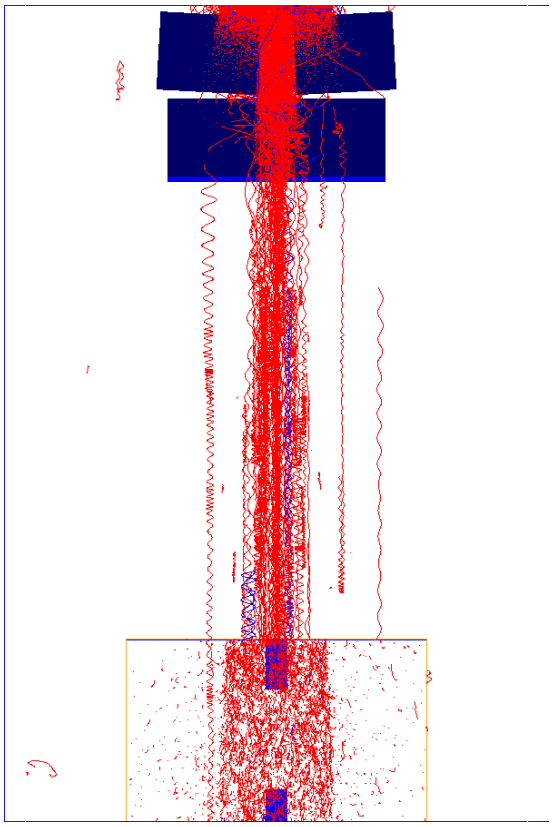

(c) $B_{MRI} = 1$ T, $B_{FF} = 1/r^5$

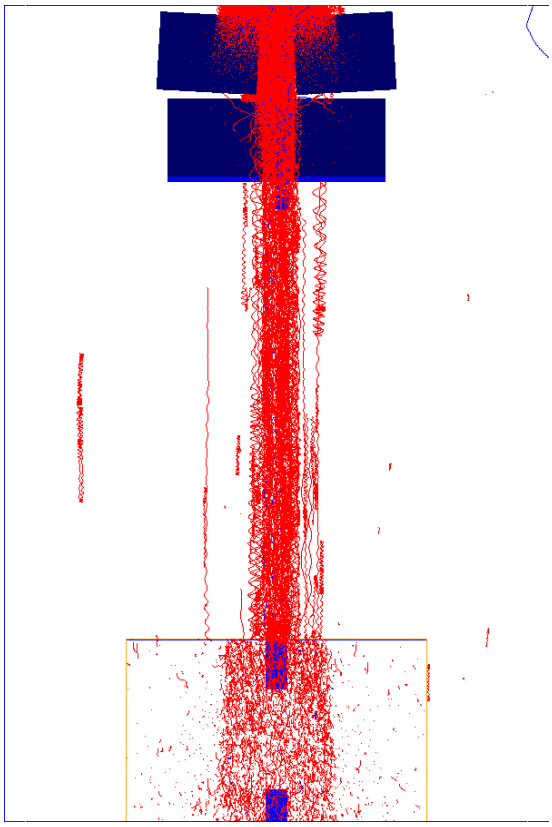

(d) $B_{MRI} = 1$ T, $B_{FF} = 1/r^2$

Figure 4: Electron contamination paths in the integrated system (100 cm isocentre with MRI coil thickness of 20 cm). In (a) we see the paths in zero magnetic field. There is moderate lateral spreading of the electrons as they travel towards the phantom. (b) shows the 0 T fringe field. Immediately as the electrons enter the region inside the coil, they are forced to travel parallel to the z-axis direction, resulting in a relatively higher concentration within the x-ray beam area, as compared to the B = 0 T case. In (c) and (d), we see the effects of a $1/r^5$ and $1/r^2$ drop-off fringe fields. The concentration of electron contamination within the x-ray beam area increases, leading to skin dose increases. The region above the patient surface contains a magnetic field of B_{MRI}, indicating the presence of the surrounding MRI coil.

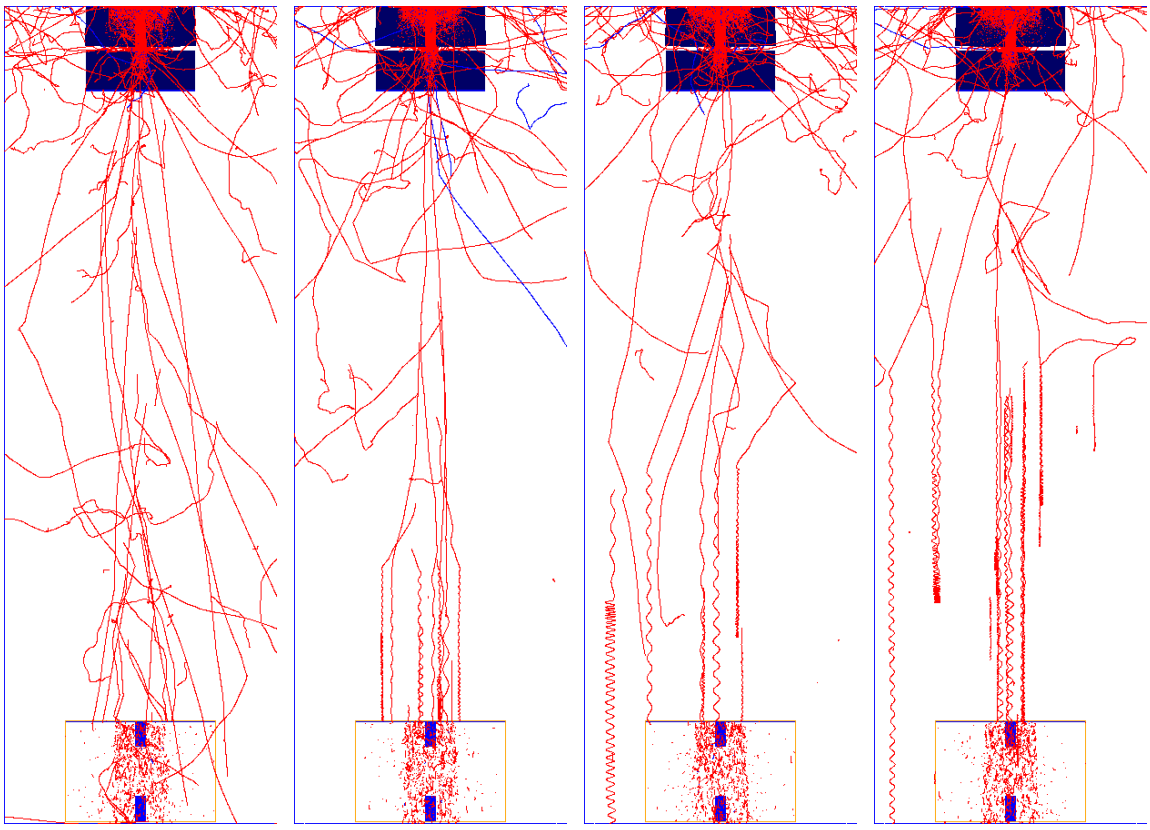

(a) B = 0 T (b) 20 cm Coil, $B_{FF} = 0$ T (c) 40 cm Coil, $B_{FF} = 0$ T (d) 60 cm Coil, $B_{FF} = 0$ T

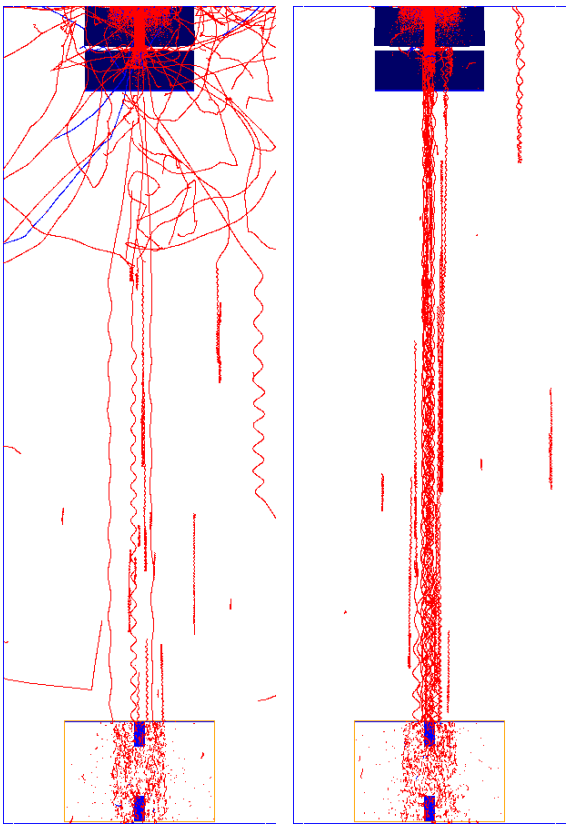

(e) 80 cm Coil, $B_{FF} = 0$ T (f) 80 cm Coil, $B_{FF} = 1/r^5$

Figure 5: Electron contamination paths in the separated system (180 cm isocentre with different MRI coil thickness ranging from 20 to 80 cm). The field size is 10x10 cm^2 and $B_{MRI} = 1$ T when applied. In (a) we see the paths in zero magnetic field. Parts (b), (c), (d) and (e) show 20, 40, 60 and 80 cm coil thickness with a 0 T fringe field. In (f), we see the effects of a $1/r^5$ fringe field with a 80 cm coil thickness.

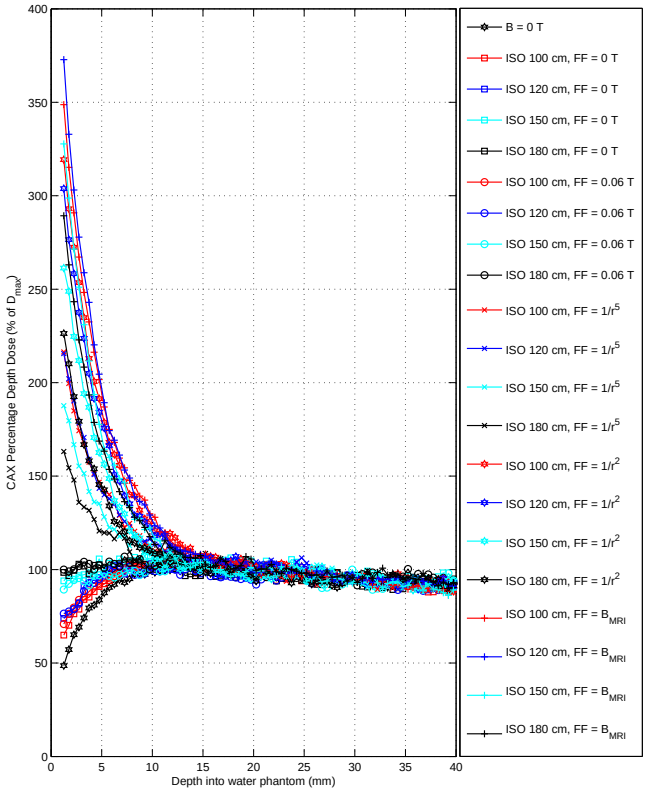

(a) CAX PDD, 5x5 cm^2, 1 T

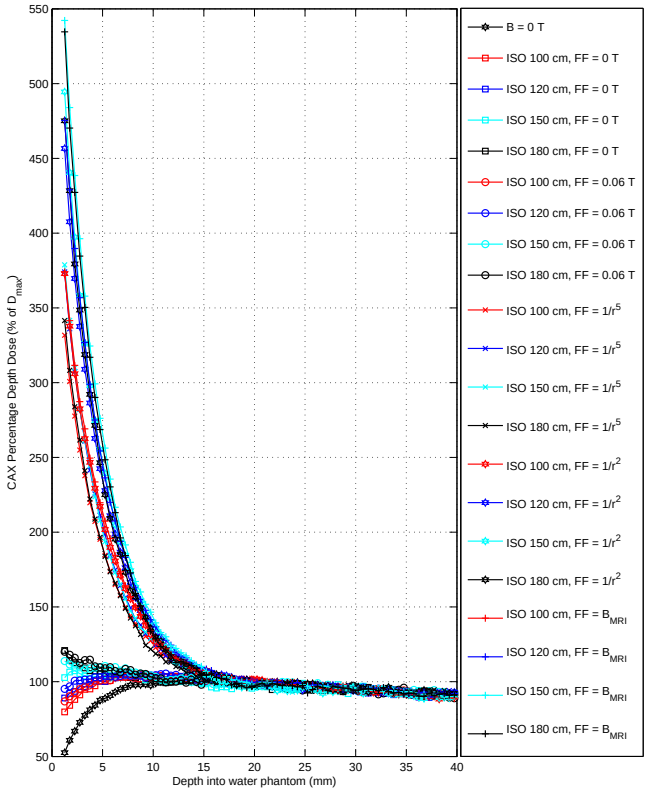

(b) CAX PDD, 10x10 cm^2, 1 T

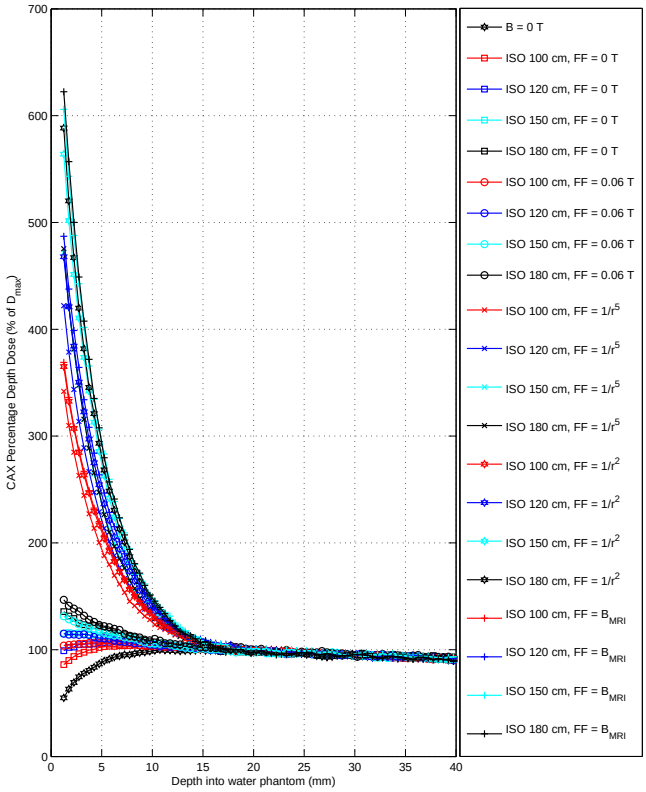

(c) CAX PDD, 15x15 cm^2, 1 T

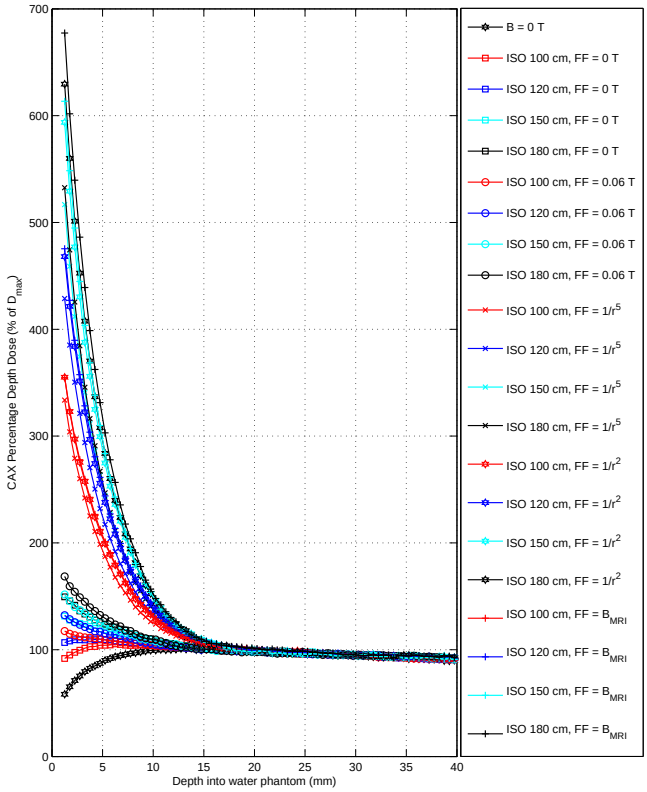

(d) CAX PDD, 20x20 cm^2, 1 T

Figure 6: Central axis PDD profiles in the first 40 mm depth for the integrated systems. Voxels in the first 1 mm are absent as the high resolution surface films are located there.

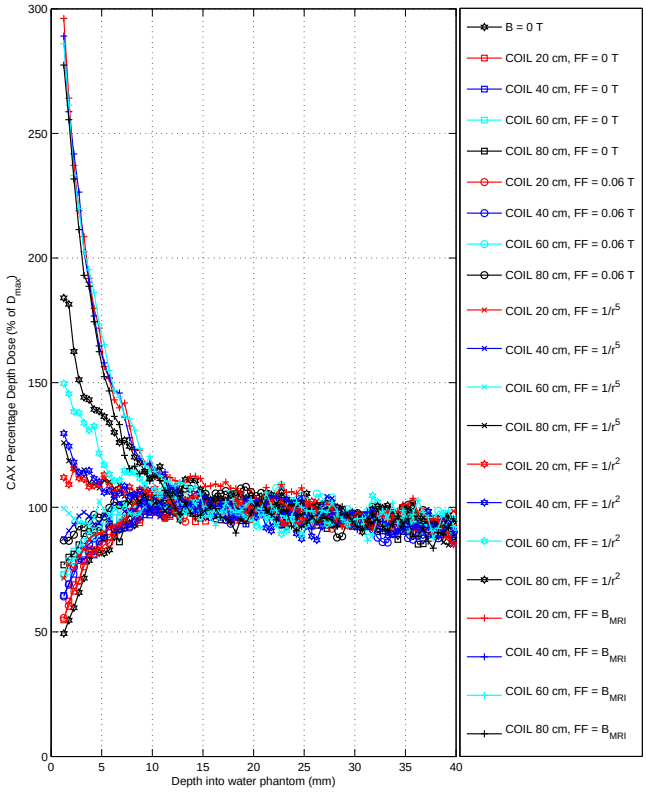

(a) CAX PDD, 5x5 cm^2, 1 T

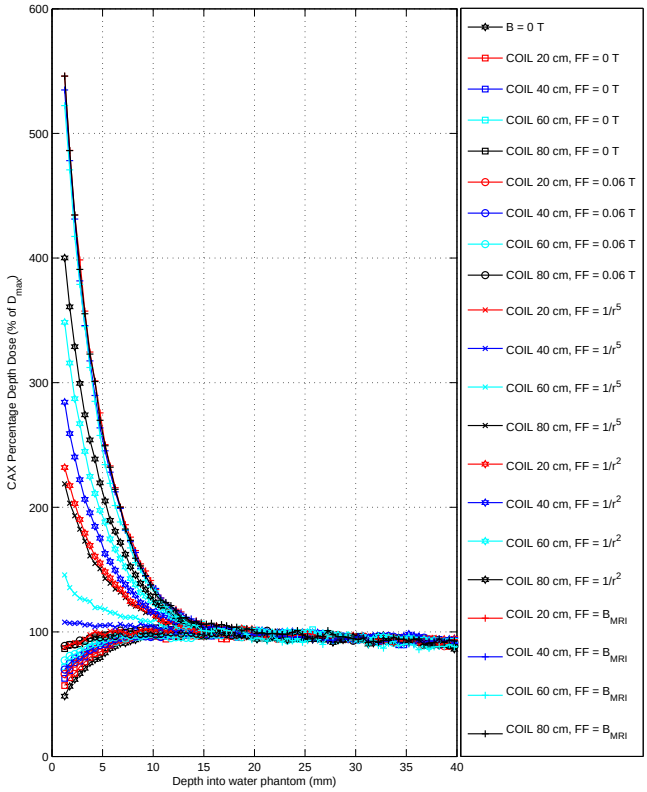

(b) CAX PDD, 10x10 cm^2, 1 T

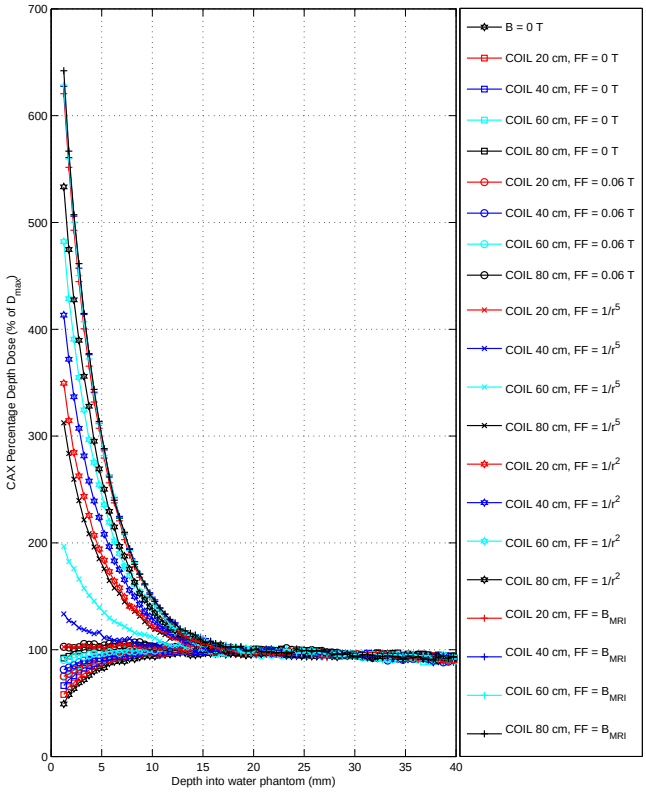

(c) CAX PDD, 15x15 cm^2, 1 T

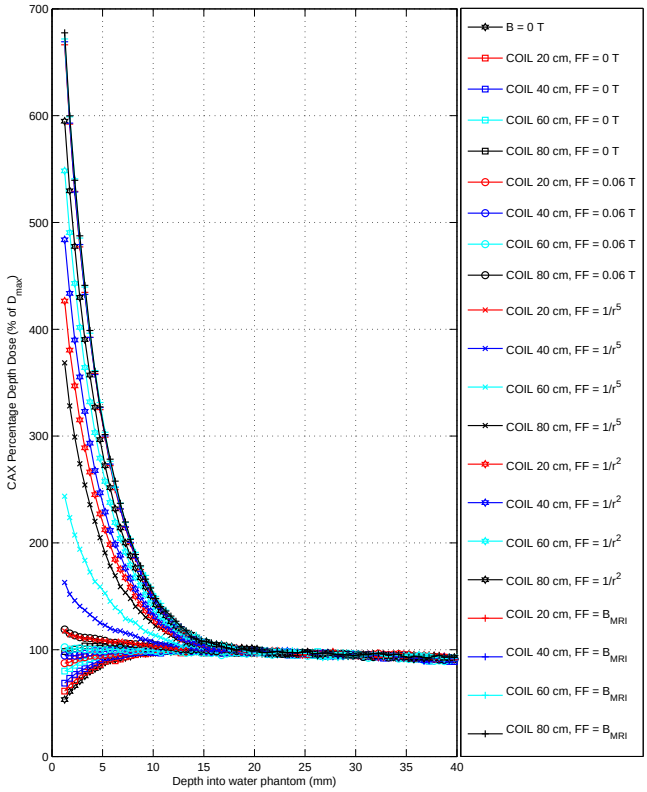

(d) CAX PDD, 20x20 cm^2, 1 T

Figure 7: Central axis PDD profiles in the first 40 mm depth for the separated systems. Voxels in the first 1 mm are absent as the high resolution surface films are located there.

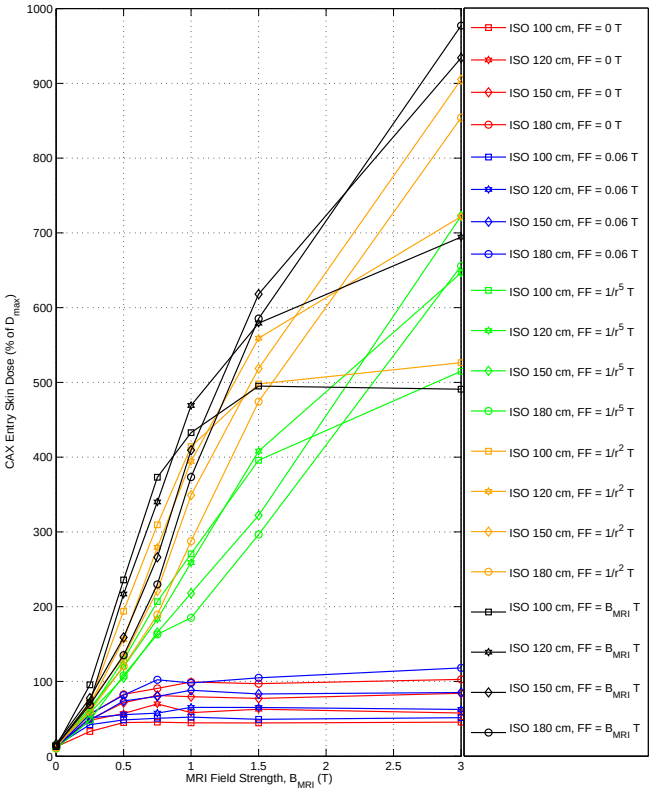

(a) 5x5 cm^2

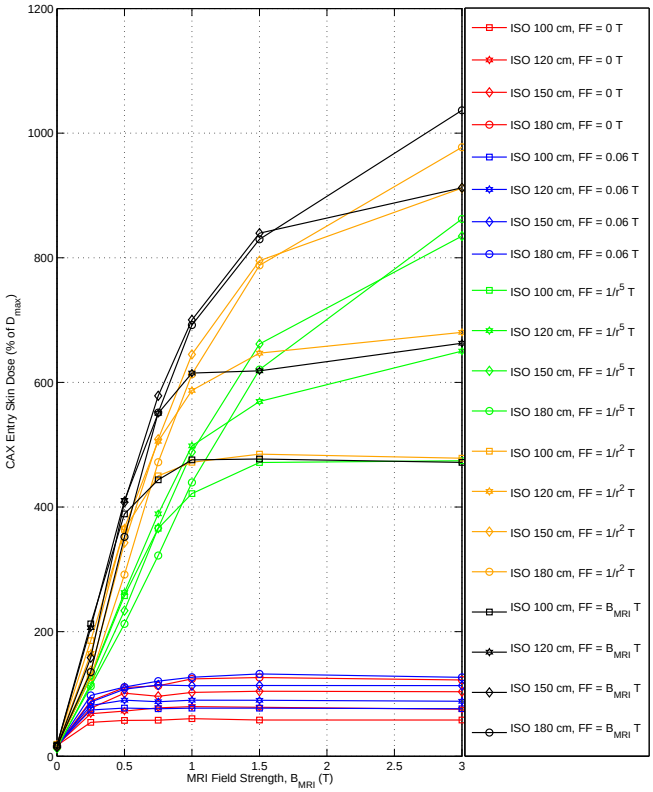

(b) 10x10 cm^2

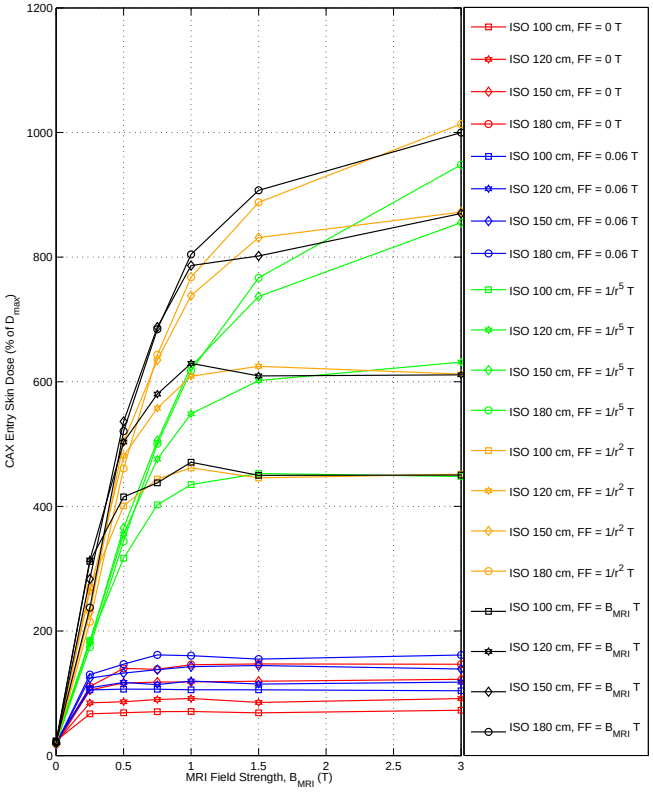

(c) 15x15 cm^2

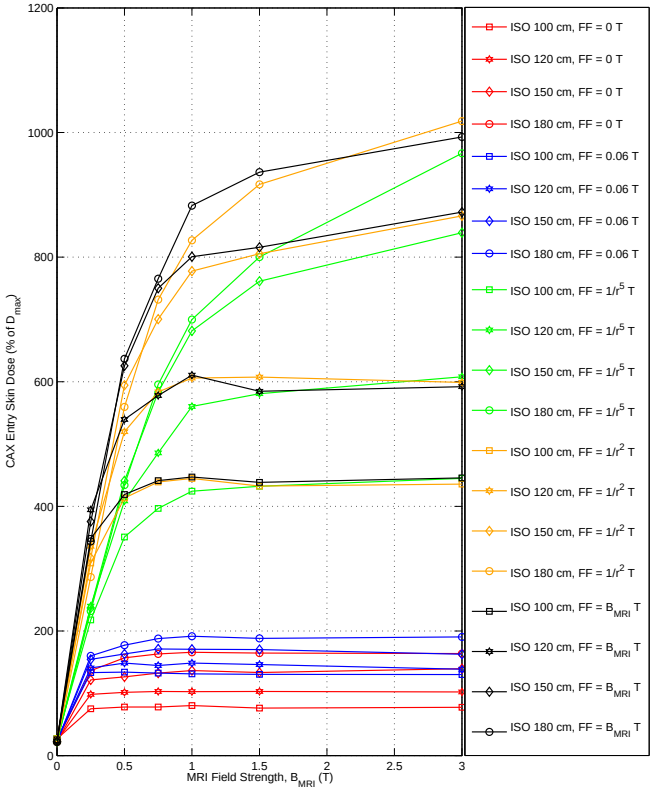

(d) 20x20 cm^2

Figure 8: Central axis entry 70 μm skin dose summary for the integrated systems. Dramatic CAX skin dose increases are reported for the fringe fields reflecting non-shielded designs ($B_{FF} = 1/r^5$, $1/r^2$, and B_{MRI}) while clinically significant increases are still reported at the shielded fringe fields of $B_{FF} = 0$ T and 0.06 T. This effect is stronger for larger field sizes as more contamination is inherent. In each of the shielded cases the skin dose increase reaches a maximum at near 0.5 T. This indicates an almost complete capturing of electron contamination with resultant minimal lateral spread. In any case, where the skin dose is greater than 100% (i.e. D_{max} it would make sense to apply sufficient entry bolus to lower the skin dose back to 100% of D_{max}. In these cases, the entire skin sparing effect of the megavoltage x-ray beam is lost.

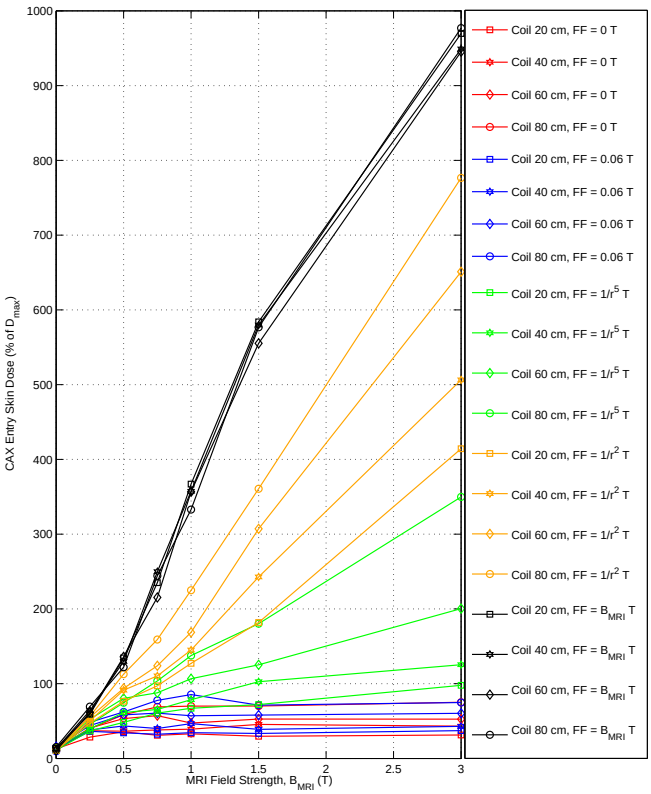

(a) 5x5 cm^2

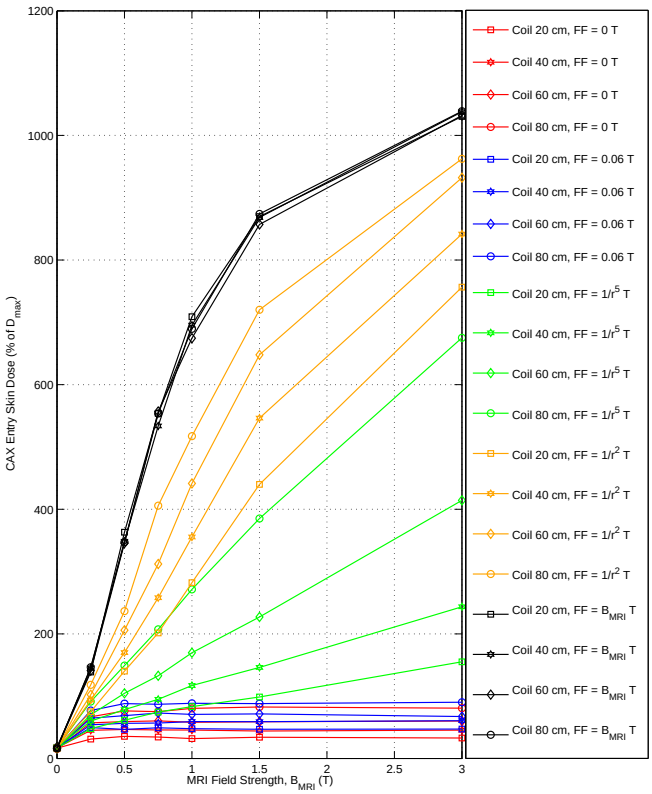

(b) 10x10 cm^2

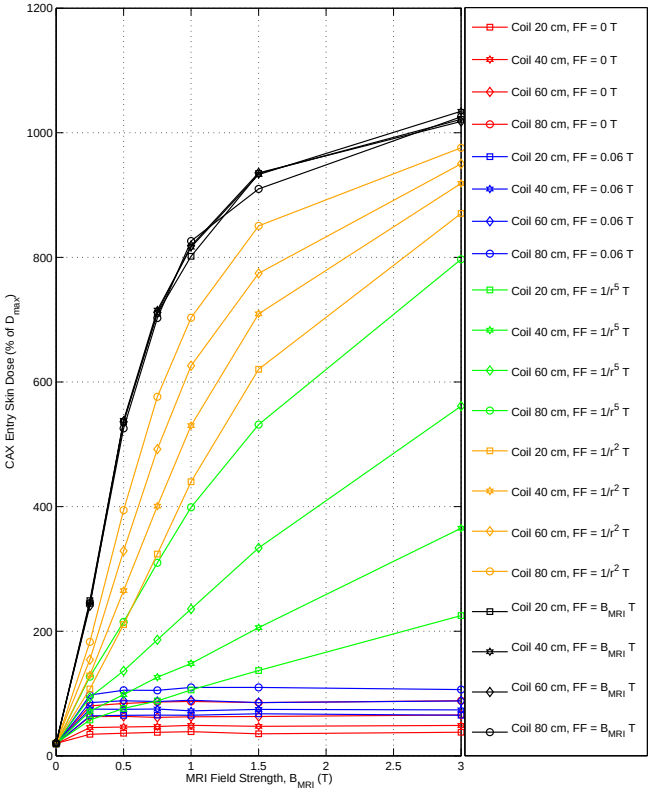

(c) 15x15 cm^2

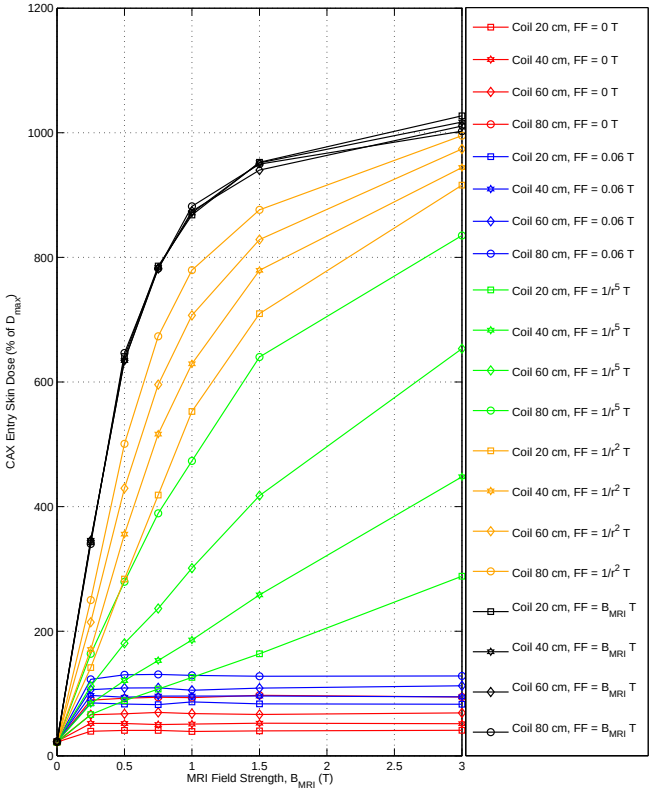

(d) 20x20 cm^2

Figure 9: Central axis entry 70 μm skin dose summary for the separated 180 cm isocentre distance system. The MRI coil thickness is varied between 20, 40, 60 and 80 cm as shown in parts a-d. Similar to figure 8, there are considerable skin dose increases at CAX for the non-shielded fringe fields and the 0.06 T fringe fields. For the fully shield case (B_{FF} = 0 T), the skin dose increase is minimal for 20 and 40 cm coil thicknesses. At 60 and 80 cm coil thickness, the increase becomes more clinical relevant. All B_{MRI} curves should allign as they are simulations with identical features.

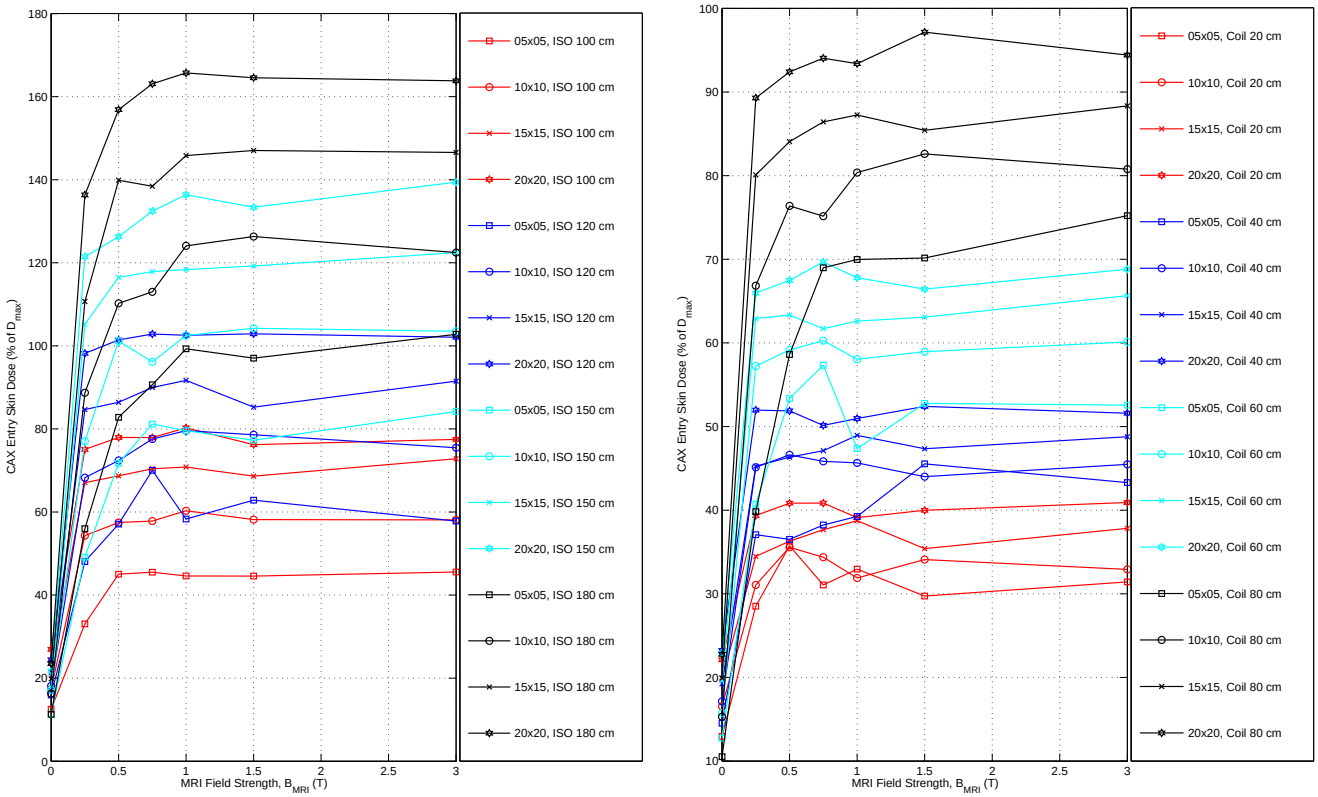

(a) Full shielded Integrated System

(b) Full shielded Separated System

Figure 10: Central axis entry 70 μm skin dose summary for the integrated and separated 180 cm isocentre distance systems with full magnetic shielding of the collimation system, i.e. $B_{FF} = 0$ T.

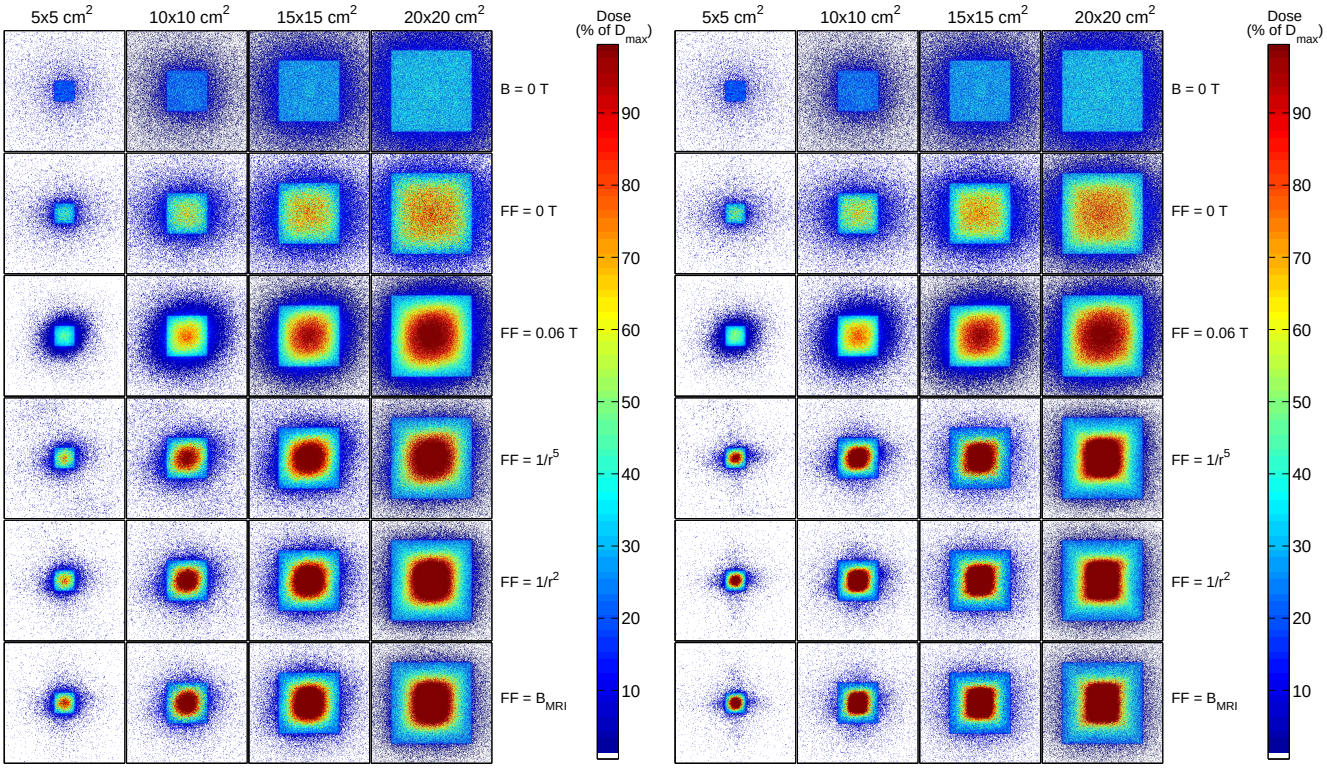

(a) B_{MRI} = 0.25 T

(b) B_{MRI} = 0.50 T

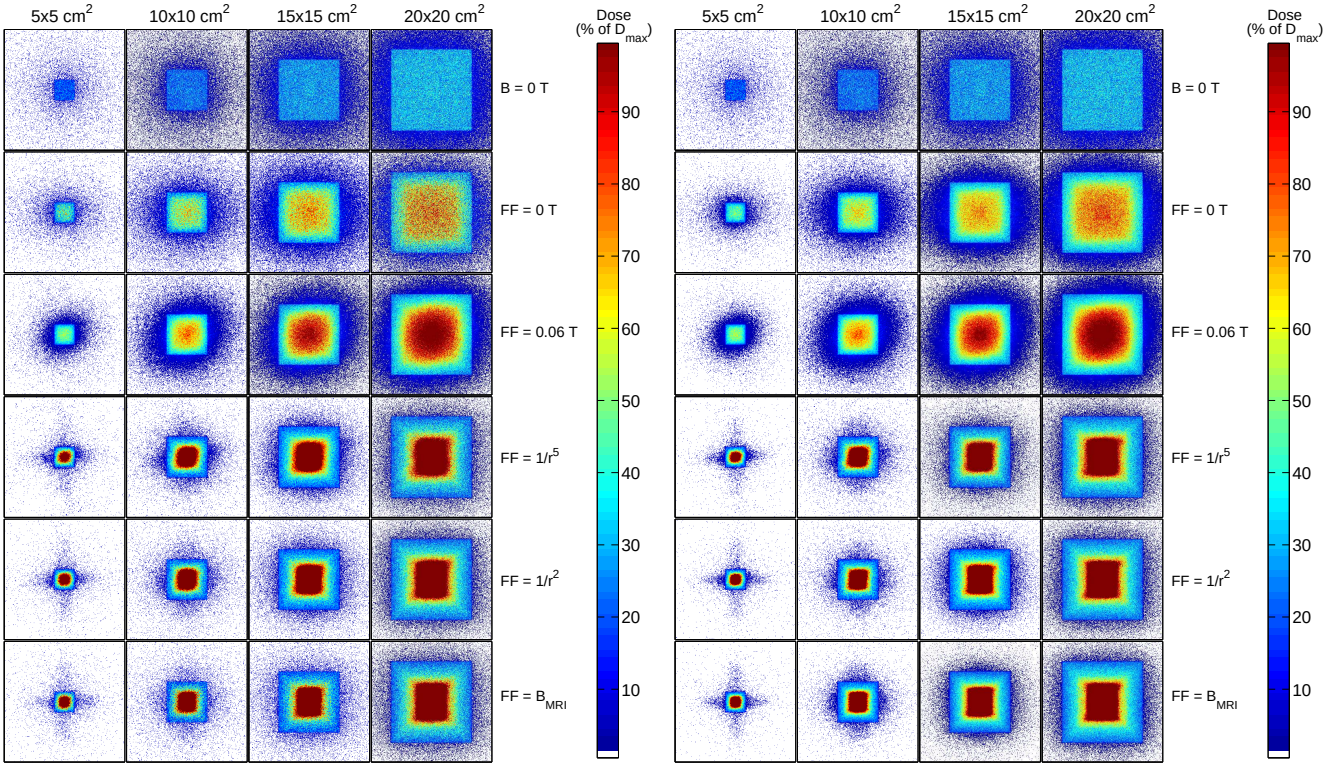

(c) B_{MRI} = 0.75 T

(d) B_{MRI} = 1.00 T

Figure 11: Entry skin dose virtual films summary for the integrated system (100 cm isocentre, 20 cm coil thickness). The B_{MRI} fields are 0.25, 0.50, 0.75, and 1 T. At B_{MRI} = 1.5 and 3 T the films are almost identical to the B_{MRI} = 1 T films. For the systems of isocentre = 120, 150 and 180 cm, the films show even further skin dose increases. The only other distinct change is the size of the CAX hot spot, which decreases with increasing isocentre distance.

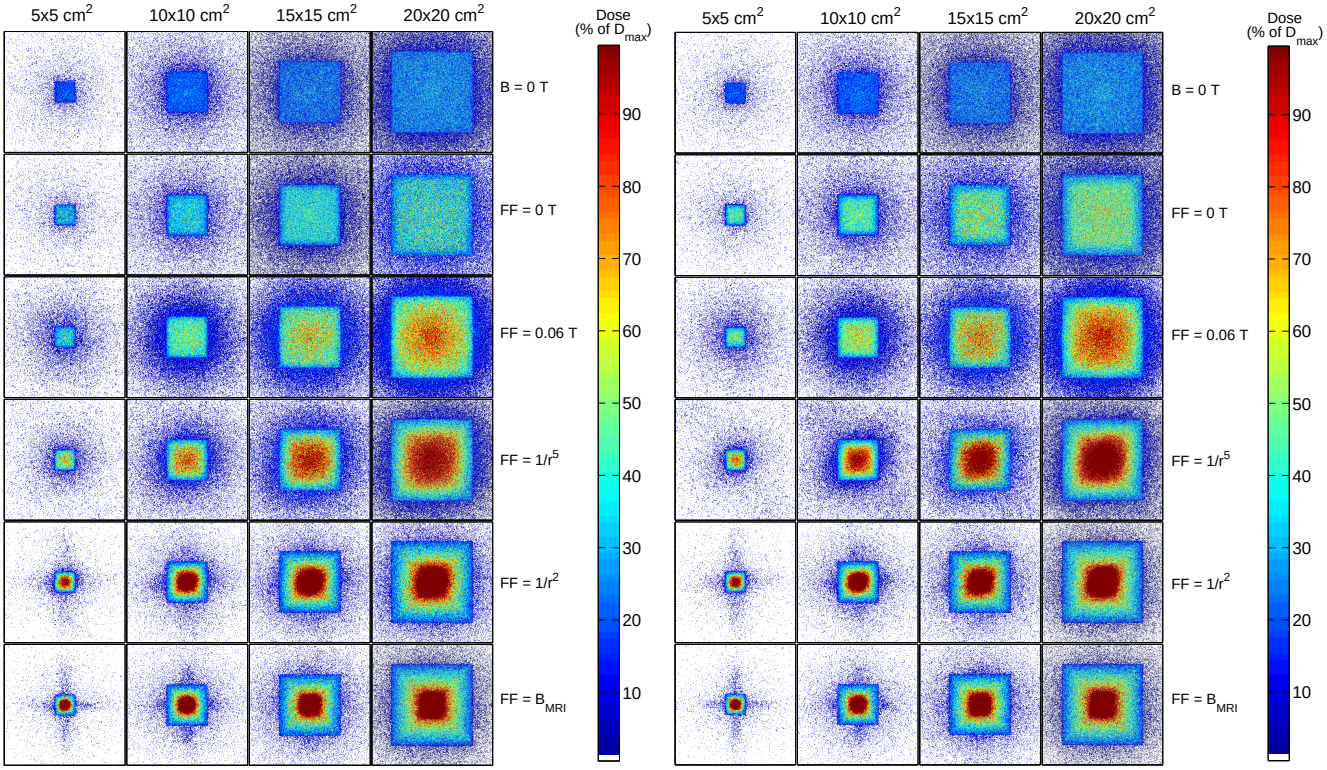

(a) 20 cm coil

(b) 40 cm coil

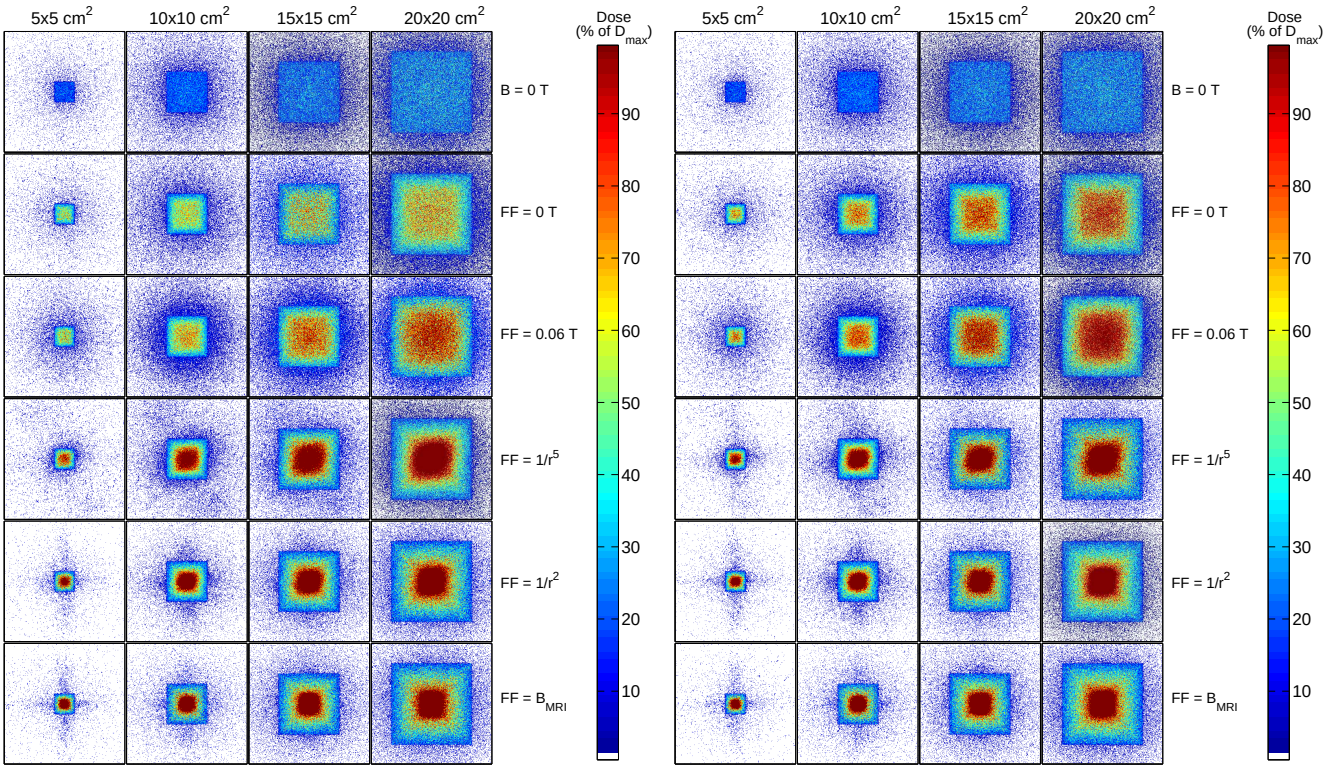

(c) 60 cm coil

(d) 80 cm coil

Figure 12: Entry skin dose virtual films summary for the separated system (180 cm isocentre) at $B_{MRI} = 1$ T.

References

[1] B W Raaymakers, J J W Lagendijk, J Overweg, J G M Kok, A J E Raaijmakers, E M Kerkhof, R W van der Put, I Meijsing, S P M Crijns, F Benedosso, M van Vulpen, C H W de Graaff, J Allen, and K J Brown. Integrating a 1.5 T MRI scanner with a 6 MV accelerator: proof of concept. *Phys. Med. Biol.*, 54:N229–N237, 2009.

[2] B. Fallone, M. Carlone, B. Murray, S. Rathee, T. Stanescu, S. Steciw, K. Wachowicz, and C. Kirkby. Development of a linac-MRI system for real-time ART. *Med. Phys.*, 34:2547, 2007.

[3] http://www.viewray.com. accessed October 2010.

[4] B. W. Raaymakers, A. J. E. Raaijmakers, A. N. T. J. Kotte, D. Jette, and J. J. W. Lagenddijk. Integrating a MRI scanner with a 6 MV radiotherapy accelerator: dose deposition in a transverse magnetic field. *Phys. Med. Biol.*, 49:4109–4118, 2004.

[5] A. J. E. Raaijmakers, B. W. Raaymakers, and J. J. W. Lagendijk. Integrating a MRI scanner with a 6 MV radiotherapy accelerator: dose increase at tissue-air interfaces in a lateral magnetic field due to returning electrons. *Phys. Med. Biol.*, 50:1363–1376, 2005.

[6] A. J. E. Raaijmakers, B. W. Raaymakers, S. van der Meer, and J. J. W. Lagendijk. Integrating a MRI scanner with a 6 MV radiotherapy accelerator: impact of the surface orientation on the entrance and exit dose due to the transverse magnetic field. *Phys. Med. Biol.*, 52:929–939, 2007.

[7] A. J. E. Raaijmakers, B. W. Raaymakers, and J. J. W. Lagendijk. Experimental verification of magnetic field dose effects for the MRI-accelerator. *Phys. Med. Biol.*, 52:4283–4291, 2007.

[8] A. J. E. Raaijmakers, B. W. Raaymakers, and J. J. W. Lagendijk. Magnetic-field-induced dose effects in MR-guided radiotherapy systems: dependence on the magnetic field strength. *Phys. Med. Biol.*, 53:909–923, 2008.

[9] C. Kirkby, T. Stanescu, S. Rathee, M. Carlone, B. Murray, and B. G. Fallone. Patient dosimetry for hybrid MRI-radiotherapy systems. *Med. Phys.*, 35(3):1019–1027, 2008.

[10] B. M. Oborn, P. E. Metcalfe, M. J. Butson, and A. B. Rosenfeld. Monte Carlo characterization of skin doses in 6 mv transverse field mri-linac systems: Effect of field size, surface orientation, magnetic field strength, and exit bolus. *Medical Physics*, 37(10):5208–5217, 2010.

[11] B. M. Oborn, P. E. Metcalfe, M. J. Butson, and A. B. Rosenfeld. High resolution entry and exit Monte Carlo dose calculations from a linear accelerator 6 MV beam under influence of transverse magnetic fields. *Med. Phys.*, 36(8):3549–3559, 2009.

[12] J St Aubin, S Steciw, and B G Fallone. Effect of transverse magnetic fields on a simulated in-line 6 mv linac. *Physics in Medicine and Biology*, 55(16):4861, 2010.

[13] J. St. Aubin, S. Steciw, and B. G. Fallone. Waveguide detuning caused by transverse magnetic fields on a simulated in-line 6 mv linac. *Medical Physics*, 37(9):4751–4754, 2010.

[14] J. St. Aubin, S. Steciw, and B. G. Fallone. Magnetic decoupling of the linac in a low field biplanar linac-mr system. *Medical Physics*, 37(9):4755–4761, 2010.

[15] J. Yun, J. St. Aubin, S. Rathee, and B. G. Fallone. Brushed permanent magnet dc mlc motor operation in an external magnetic field. *Medical Physics*, 37(5):2131–2134, 2010.

[16] C. Kirkby, B. Murray, S. Rathee, and B. G. Fallone. Lung dosimetry in a linac-mri radiotherapy unit with a longitudinal magnetic field. *Medical Physics*, 37(9):4722–4732, 2010.

[17] A. F. Bielajew. The effect of strong longitudinal magnetic fields on dose deposition from electron and photon beams. *Med. Phys.*, 20:1171–1179, 1993.

[18] T. N. Padikal and J. A. Deye. Electron contamination of a high-energy x-ray beam. *Phys. Med. Biol.*, 23:1086–1092, 1978.

[19] P. J. Biggs and C. C. Ling. Electrons as the cause of the observed shift in dmax with field size in high energy photon beams. *Med. Phys*, 6:p291–295, 1979.

[20] B. Nilsson and A. Brahme. Absorbed dose from secondary electrons in high energy photon beams. *Phys. Med. Biol.*, 24:901–912, 1979.

[21] C. C. Ling, M. C. Schell, and S. N. Rustgi. Magnetic analysis of the radiation components of a 10MV photon beam. *Med. Phys.*, 9:20–26, 1982.

[22] P. J. Biggs and M. D. Russell. An investigation in the presents of secondary electrons in megavoltage photon beams. *Phys. Med. Biol.*, 28:1033–1043, 1983.

[23] P. L Petti, M. S. Goodman, J. S. Sisterson, P. J. Biggs, T. A. Gabriel, and R. Mohan. Sources of electron contamination for the Clinac-35 25MV photon beam. *Med. Phys.*, 10:856–861, 1983.

[24] G. Krithivas and S. N. Rao. A study of the charcteristics of radiation contaminants within a clinically useful photon beam. *Med. Phys.*, 12:764–768, 1985.

[25] E. D. Yorke, C. C. Ling, and S. Rustgi. Air-generated electron contamination of 4 and 10MV photon beams: a comparison of theory and experiment. *Phys. Med. Biol.*, 30:1305–1314, 1985.

[26] R. Sjogren and M. Karlsson. Electron contamination in high energy photon beams. *Med. Phys.*, 23(11):1873–1881, 1996.

[27] T. C. Zhu and J. R. Palta. Electron contamination in 8 and 18 MV photon beams. *Med. Phys.*, 25(1):12–19, 1997.

[28] Antonio Lopez Medina, Antonio Teijeiro, Juan Garcia, Jorge Esperon, J. Antonio Terron, Diego P. Ruiz, and Maria C. Carrion. Characterization of electron contamination in megavoltage photon beams. *Med. Phys.*, 32(5):1281–1292, 2005.

[29] N. Damrongkijudom, B. Oborn, M. Butson, and A. Rosenfeld. Measurement and production of electron deflection using a sweeping magnetic device in radiotherapy. *Australas. Phys. Eng. Sci. Med.*, 29 (3):260–266, 2006.

[30] D. W. Litzenberg, B. A. Fraass, D. L. McShan, T. W. ODonnel, D. A. Roberts, F. D. Becchetti, A. F. Bielajew, and J. M. Moran. An apparatus for applying strong longitudinal magnetic fields to clinical photon and electron beams. *Phys. Med. Biol.*, 46:N105115, 2001.

[31] Yu Chen, Alex F. Bielajew, Dale W. Litzenberg, Jean M. Moran, and Frederick D. Becchetti. Magnetic confinement of electron and photon radiotherapy dose: A monte carlo simulation with a nonuniform longitudinal magnetic field. *Medical Physics*, 32(12):3810–3818, 2005.

[32] University of Alberta Cross Cancer Institute(CCI). The Linac-MR Project. *http://www.mp.med.ualberta.ca/linac-mr/*, 2008.

[33] J. D. Jackson. *Classical Electrodynamics, 3rd Edition.*

[34] S. Agostinelli et al. Geant4-a simulation toolkit. *Nucl. Instrum. Methods Phys. Res. A*, 506:250–303, 2003.

[35] Varian Medical Systems. Palo Alto, CA.

[36] International Commission on Radiological Protection. ICRP Publication 59, The Biological Basis for Dose Limitation in the Skin. *Annals of the ICRP*, 22(2), 1992.

[37] S. Devic, J. Seuntjens, W. Abdel-Rahman, M. Evans, M. Olivares, E. B. Podgorsak, Te Vuong, and C. G. Soares. Accurate skin dose measurements using radiochromic film in clincal applications. *Med. Phys.*, 33(4):1116–1124, April 2006.